Title
EMISSION OF COMPLEX FRAGMENTS FROM HIGHLY EXCITED SYSTEMS PRODUCED IN 93Nb + 9Be AND 27Al REACTIONS AT E/A =25.4 AND 30.3 MeV

Author
Charity, R.J.

Publication Date
1987-06-01

LBL-22447
Preprint c. 2

Lawrence Berkeley Laboratory
UNIVERSITY OF CALIFORNIA

Submitted to Nuclear Physics A

EMISSION OF COMPLEX FRAGMENTS FROM HIGHLY EXCITED SYSTEMS PRODUCED IN $^{93}Nb + {}^{9}Be$ AND ^{27}Al REACTIONS AT E/A = 25.4 AND 30.3 MeV

R.J. Charity, D.R. Bowman, Z.H. Liu, R.J. McDonald,
M.A. McMahan, G.J. Wozniak, L.G. Moretto,
S. Bradley, W.L. Kehoe, and A.C. Mignerey

June 1987

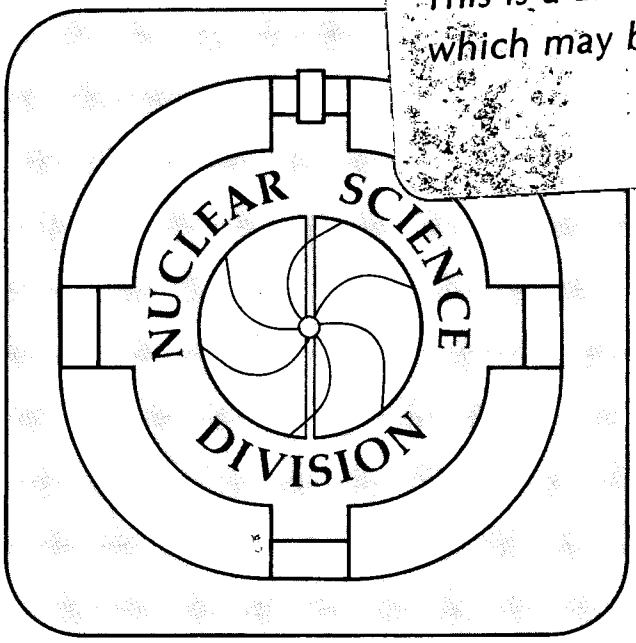

Prepared for the U.S. Department of Energy under Contract DE-AC03-76SF00098

DISCLAIMER

LBL-22447

Emission of Complex Fragments from Highly Excited Systems Produced in $^{93}Nb + ^{9}Be$ and ^{27}Al Reactions at E/A = 25.4 and 30.3 MeV

R.J. Charity, D.R. Bowman, Z.H. Liu,[1] R.J. McDonald, M.A. McMahan, G.J. Wozniak, L.G. Moretto, S. Bradley,[2,3] W.L. Kehoe,[3] A.C. Mignerey[3]

Nuclear Science Division
Lawrence Berkeley Laboratory
University of California
Berkeley, California 94720

June 1987

1 Permanent Address: Institute of Atomic Energy, Beijing, China
2 Present Address: Kaman Sciences, 2560 Huntington Ave., Alexandria, VA 22303
3 Department of Chemistry, University of Maryland, College Park, MD 20742

This work was supported by the Director, Office of Energy Research, Division of Nuclear Physics of the Office of High Energy and Nuclear Physics of the U.S. Department of Energy under Contract DE-AC03-76SF00098.

June 5th 1987
LBL-22447

EMISSION OF COMPLEX FRAGMENTS FROM HIGHLY EXCITED SYSTEMS PRODUCED IN ^{93}Nb + ^{9}Be AND ^{27}Al REACTIONS AT E/A = 25.4 AND 30.3 MeV.

R.J. CHARITY, D.R. BOWMAN, Z.H. LIU[a], R.J. McDONALD, M.A. McMAHAN, G.J. WOZNIAK, and L.G. MORETTO

Nuclear Science Division, Lawrence Berkeley Laboratory, University of California, Berkeley, California, 94720, USA.

S. BRADLEY[b], W.L. KEHOE, and A.C. MIGNEREY

Department of Chemistry, University of Maryland, College Park, Maryland, 20742, USA

Abstract: Complex fragments with atomic numbers intermediate between that of the target and projectile have been detected in the reverse-kinematics reactions of ^{93}Nb plus ^{9}Be and ^{27}Al at bombarding energies of E/A = 25.4 and 30.3 MeV. Experimental results from inclusive and coincidence measurements are presented and are used to characterize these fragments as the statistical, binary decay products of highly excited compound nuclei formed in fusion-like reactions.

NUCLEAR REACTIONS Be,Al(Nb,X), E = 25.4, 30.3 MeV/nucleon; measured fragment σ(fragment,E_X,θ), fragment-fragment coin.;deduced reaction mechanism. Statistical model calculations.

(a) Permanent address: Institute of Atomic Energy, Beijing, China.

(b) Present address: Kaman Sciences, 2560 Huntington Ave., Alexandria, VA 22303.

1. Introduction

Low energy heavy-ion collisions, extending in energy from the neighborhood of the Coulomb barrier up to a few MeV/nucleon, are very gentle interactions in which a few low frequency degrees of freedom play a dominant role. In these processes, the main issue is whether the dinuclear system manages to fuse (giving rise to a compound nucleus) or having failed to do so, whether it reseparates into two fragments with charge, mass, energy, and angular momentum transfers characteristic of a deep-inelastic collision.

The time evolution of the dinuclear system occurs in a multidimensional space consisting of relative distance, mass and charge asymmetry, a few shape degrees of freedom, and a few angular momentum bearing modes. In these coordinates, a paramount role is played by the potential energy and by the viscosity tensor which, each in its own way, keep the kinetic energy under rather tight control. As a result of this delicate interplay of kinetic energy, potential energy and viscosity, the amount of fusion strongly depends upon the kinetic energy and effective fissility of the system, while deep-inelastic processes are characterized by large energy and angular momentum dissipations and by large thermal-like fluctuations.

As one progresses towards higher energies, in the range of 10 to 100 MeV/nucleon, now identified as the intermediate-energy regime, one should observe a variety of changes taking place. From a purely macroscopic point of view, one expects an increasing dominance of inertial effects associated with the increased kinetic energy in the entrance channel, and a declining role of those modes characterized either by low frequency or by long relaxation times, or by both. A peculiar but straightforward consequence of this state of affairs is a possible simplification of the primary macroscopic reaction mechanism due to the progressive disappearance of many degrees of freedom relevant at lower energies, like mass asymmetry, shape degrees of freedom, and intrinsic angular momentum modes.

An extreme simplification suggested by experiment could be the following: for a given impact parameter either occluded volume of the two overlapping spheres (target and projectile) may be sheared away in the collision, the energy of the newly created surface, as well as the inertias of the relevant pieces, determining which of the two occluded pieces will be sheared off [1]). The sheared-off piece may then amalgamate with the intact partner to produce an incomplete-fusion product, while the residue of the

abraded partner tends to retain its motion, less and less perturbed by the shearing action, the faster the shearing process becomes. Asymmetric systems are more susceptible to this kind of reaction, the smaller nucleus bearing the brunt of the shearing process.

Figure 1 shows the predicted impact parameters, as a function of bombarding energy, at which the breakup of either the target or the projectile is possible in the reaction Nb + Be. These impact parameters were calculated using the model of Ref. 1. For each impact parameter, there is a lower energy limit below which neither of the two occluded parts can be sheared off. This sets the lower limit of the breakup processes and the upper limit of complete fusion-deep inelastic processes. This limit moves to lower energies with increasing impact parameter for obvious geometric reasons. At the largest impact parameters these shear-off processes can occur at very low energies, and are known as direct or quasi-elastic reactions. At the upper energy range, incomplete fusion ends. The process ceases to be binary, as both occluded pieces can be sheared off their respective parents. This gives rise to the so called and better explored fireball regime characterized by a hot intermediate (fireball) formed by the amalgamation of the two occluded regions, and by the two spectator pieces [2]). With these general qualitative ideas in mind, one can proceed to explore the experimental situation as it has developed in the past few years.

Prompted by preliminary results with first generation heavy ion machines, a large amount of work has been performed on the subject of linear momentum transfer by measuring fission-fragment folding angle distributions [3-5]). The observed momentum transfer, which is complete at lower energies, progressively becomes more incomplete as the bombarding energy increases. This is in general accordance with the incomplete fusion model outlined above although this model is by no means completely accepted. Difficulties in characterizing the fissioning system, among other things, prevent one from establishing a direct correlation between impact parameter, mass transfer and momentum transfer.

Similar trends in the measured momentum transfer as a function of bombarding energy have been obtained in studying the evaporation residues [6-8]). Heavy forward-moving products suggest the formation of hot compound nuclei in an incomplete fusion process, which undergo massive evaporation, leaving behind heavy remnants.

Complex fragments with masses intermediate between alpha particles and fission fragments are also produced in fair abundance in intermediate-energy reactions. However, some difficulty has been encountered in determining their origin and the mechanism of their production. A putative power-law dependence of their mass (or charge) distribution [9-15]) has prompted some authors to associate them with a liquid-vapor phase transition [16]) or, more precisely with the critical opalescence occurring in the vicinity of the critical point. This belief has lead to an experimental inference of the critical temperature and density and has promoted a revival of the Fisher theory of droplet condensation [17]) by a number of theorists [18-20]). More daring authors have identified the process as a cold fragmentation [21]) or shattering of nuclei under shock in analogy with the shattering of glass or other suitably brittle material. In this, as in the previous cases, the inclusive mass distribution was adequately fit by the theory. An inspection of the associated kinetic energy spectra is not very conclusive. The spectra can be parameterized in terms of emission from moving source(s) [14-15]). However, the interpretation of the fitted parameters is not clear.

The thermal-like behavior of the kinetic energy spectra and yields of complex fragments in high energy proton induced reactions [9,10,13]) has led to the recognition that compound nuclei can in fact emit the whole range of complex fragments from ^{4}He to fission fragments. One theory that arose [22]) was formulated as a generalization of fission with explicit treatment of the mass asymmetry degree of freedom. For any given mass asymmetry, it is possible to find a constrained or conditional saddle-point that, like the ordinary saddle-point in fission, controls the decay rate at that particular asymmetry. The locus of the conditional saddles constitutes the ridgeline whose energy profile determines, together with the excitation energy or temperature, the shape of the mass distribution. In recent experiments [23-25]), the low energy emission of complex fragments has been characterized as a true compound nucleus process and the associated conditional barriers have been extracted and used to test recent refinements in the liquid-drop model [26]).

The experimental confirmation of the compound nucleus origin of complex fragments at low bombarding energy leads to the fact that the emission probability of these fragments should rapidly increase with increasing excitation energy. In particular, if very hot nuclei were produced in intermediate-energy reactions, they would decay rather abundantly by the emission of complex fragments. This can be

readily understood from the Boltzman-like dependence of the decay width Γ upon the potential energy V and the saddle-point temperature T, namely $\Gamma \alpha \exp(-V/T)$. An example of this feature is given in Fig. 2 where it is shown qualitatively how the fragment yields are expected to depend on the excitation energy of the emitting system. The fragment yields increase several orders of magnitude as the excitation energy increases from 50 to 400 MeV. At the high excitation energies, the yields for all asymmetries become more comparable.

At present, there is a singular lack of compound nucleus signatures in the available intermediate-energy heavy-ion data. This confused situation can be attributed to the broad range of velocities associated with target-like and projectile-like fragments produced over a broad range of impact parameters with a related range of momentum transfers. A desirable reduction in the range of impact parameters can be achieved by using very asymmetric entrance channels. This may also help minimize or even eliminate the role of the source associated with the light partner. Furthermore, by utilizing reverse-kinematics, one can detect all of the source fragments in a relatively small laboratory angular range.

These reasons led to the choice of the reactions ^{93}Nb + ^{9}Be & ^{27}Al at 25.4 and 30.3 MeV/u in reverse-kinematics for our initial attempt to establish whether compound nucleus decay plays any role in the production of complex fragments at intermediate energies.

The paper is organized as follows: In Sec. 2, the experimental details are given. The results of the inclusive measurements are shown and discussed in Sec. 3. Coincidence measurements are presented and discussed in Sec. 4. Finally the conclusions are summarized in Sec. 5.

Part of this work has been published elsewhere [27].

2. Experimental Method

The experiment was performed at the Bevalac of the Lawrence Berkeley Laboratory. Beams of 10^7 particles per pulse of ^{93}Nb with energies of 25.4 and 30.3 MeV/u impinged on targets of ^{9}Be (2.6 mg/cm^2) and ^{27}Al (3.8 mg/cm^2). The thin targets ensured that the projectile's energy loss within the targets was small (less than 3% of the initial beam energy).

Particles were detected in two medium area E-ΔE telescopes placed on either side of the beam. The energy loss of a particle entering the telescope was measured with a gas ionization chamber and the residual energy was measured with a 2 mm thick, Li-drifted Si detector. The diameter of the active area of the Si detectors was 6.8 cm. The ionization chambers were operated with a gas mixture of 90% Ar and 10% CH_4 at a pressure of 200 torr. The telescopes were position sensitive in two dimensions. The in-plane position signal was obtained from the voltage division across a Pd resistive layer evaporated on the front surface of the Si detector. The out-of-plane position was determined from the drift time of the electrons in the gas ionization chamber. Detector 1 was centered at 5.5° and had an acceptance angle of 5°. The other telescope (Detector 2) was centered at -9° with an acceptance angle of 6°.

The energy calibration for the Si detectors was obtained using elastically scattered Nb projectiles from a 3 mg/cm^2 Au target. Calibration points were obtained with Nb beams of energy from 11.4 to 30.3 MeV/u. The lower energy beams were produced by degrading the 30.3 MeV/u beam with Al degraders. The energy loss within the degraders was calculated from the tables of Ref. 28. Corrections were made for the pulse-height-defect using the systematics of Moulton *et al.* [29]).

The gas ionization chambers were also calibrated at the same time. Measurements of the residual energy of elastically scattered beam particles, with and without gas in the ionization chamber, allowed the energy loss within the gas section to be deduced. These energy losses were used as calibration points.

Corrections were also made to account for energy losses in the Mylar window of the ionization chamber and the Au absorber foils used for suppressing electrons and X-rays. The energy calibrations were accurate to ±2%.

The position calibration was determined with a mask consisting of a matrix of 2.5 mm diameter holes separated by 5 mm. The typical position resolution obtained was ± 0.2°. However, the determination of the scattering angles was limited to an accuracy of ±0.5° due the large size of the beam spot. Cross sections were normalized with respect to the beam charge collected in a Faraday cup. Inclusive and coincidence events between the two telescopes were recorded on magnetic tape and analyzed off-line .

Figures 3 & 4 show representative E-ΔE spectra obtained with the detector at 5.5°. Ridges corresponding to different atomic numbers can be seen, especially in the spectrum for 30.3 MeV/u Nb on Al reaction. The Z resolution is less than one Z unit F.W.H.M. for atomic numbers less than 30. For the 25.4 MeV/u Nb + Be reaction, the more energetic lighter fragments ($Z < 9$) punched through the Si detector and did not deposit their full energy. The punch through-line is not evident in the 30.3 MeV/u Nb +Al spectrum due to a higher ΔE threshold .

3. Inclusive data

3.1 VELOCITY DIAGRAMS

The use of reverse-kinematic reactions provides a clear signature for the production of complex fragments by a binary decay mechanism. To illustrate this point, let us consider the kinematics diagram shown in Fig. 5a. The vector V_s represents the velocity of a system which is the source of the complex fragments. Such a system could be formed in an inelastic interaction of the target and projectile nuclei such as a complete or incomplete fusion reaction. Because of the large asymmetry of the entrance channel, the source velocity (V_s) is only slightly less than the beam velocity and hence quite large. A particular complex fragment, produced by a statistical, binary decay of the source system, is emitted with a well characterized velocity (V_e) determined mostly by the Coulomb repulsion between it and its partner. The locus of all possible emission velocity vectors (V_e) is represented by the circle in Fig. 5a. The fragments observed at a laboratory angle θ, smaller than a critical value, have two velocities (represented by vectors V_a and V_b in Fig. 5a.). The high velocity solution (V_a) corresponds to a forward emission in the center-of-mass and the low velocity solution (V_b) corresponds to backward emission in the center-of-mass. If the reaction mechanism, involved in the present reactions, does in fact produce compound nuclei with a narrow distribution of velocities, one ought to observe such double solutions. This is indeed the case in the reactions under consideration. The two solutions are clearly visible in Figs. 3 and 4.

Conversely, if complex fragments were produced in a multifragmentation process,

where typically more than two fragments are produced per event, then a particular fragment is no longer emitted with a well characterized velocity in the source frame of reference. Emission velocities ranging from zero up to the two-body decay value are possible. Hence fragments produced by multi-fragmentation should fill up the kinematic rings associated with the two-body decay events. The distribution of laboratory velocities would no longer show two distinct solutions, but would consist of events covering an extended range of velocities. The existence of two kinematic solutions for the complex fragments is thus a clear signature for a binary decay production mechanism.

In order to verify the kinematics for complex fragment emission, a velocity was derived for each detected particle. This velocity was evaluated from the particle's measured energy by assuming a single mass for each Z species. In estimating these masses, it should be stressed that the primary fragments can have large excitation energies and so sequential evaporation of light particles from these fragments is an important effect. The statistical code PACE [30]) was used to simulate this evaporation process for primary fragments with a large range of Z, A and excitation energy. The average atomic charge <Z> of the secondary fragments was found to be well correlated to their average atomic number <A>. For Z<40 the dependence of <A> on <Z> is well reproduced by the relation

$$\langle A \rangle = 2.08 \langle Z \rangle + 0.0029 \langle Z \rangle^2. \qquad (1)$$

This result was found to be independent of the initial Z, A and excitation energy as long as the excitation energy was large enough ($E^*/A > 1$ MeV). In order to gain confidence in Equation 1, one can compare its predictions against experiment. The isotope distributions of Z=8, 14 & 20 fragments produced in the similar reaction Kr + C at E/A = 35 MeV [31]) are particularly suitable for comparison as the production mechanism of these fragments is most likely the same as in the present work. Equation 1 reproduces the mean A of these distributions to within ± 0.2 mass-units. The second moment of these distributions is ≈1 mass-units. Over the range of fragments $5 \leq Z \leq 40$, Equation 1 is estimated to be accurate to within ± 0.5 mass-units. Including the uncertainty in the energy calibration, this implies a total uncertainty of

±2% in deriving the average velocities of these fragments.

Fig. 6 shows contours of the invariant cross sections in the Z-velocity plane obtained with Detector 1 at 5.5°. The dashed lines indicate the largest velocity for which fragments still stop in the Si detector. For fragments with velocities above this value, the total fragment energy was not measured. For the reactions with the Be target, an attempt was made to reconstruct the total energy of these events from their energy loss in the Si detector. This reconstruction is not very accurate, it was only done for display purposes, and was not used in any further analysis.

Both the E-ΔE maps of Figs. 3 & 4 and the contour map of the invariant cross sections in the Z-velocity plane given in Fig. 6 suggest the presence of three components. The first component is concentrated at large Z-values in the general vicinity of the projectile Z-value and is predominantly found at small angles. In fact it is visible only in the most forward setting of the telescopes. This component appears to be the evaporation residues of very hot compound nuclei whose angular distribution extends as far as the inner part of the most forward telescope. In order to verify this hypothesis, a simulation with the evaporation code PACE was performed for the 25.4 MeV/u Nb + Be reaction. A compound nucleus was assumed to be formed in an incomplete fusion reaction (initial system $A = 100$; $Z = 48$; $E^* = 148$ MeV ; $J_{max} = 42$ $\hbar$) and was allowed to evaporate. The histogram of the evaporation residue angular distribution is shown in Fig. 7. The effect of the finite angular resolution of the experiment has been included. This figure suggests that about 0.1% of the overall angular distribution was seen by our detector in its most forward angular setting.

The second component covers a much larger range of atomic numbers and is concentrated into two velocity ridges of nearly equal intensity. This component is the object of our present study and will be discussed extensively.

The third component is visible at small atomic numbers ($Z \leq 10$ for the reactions with the Be target, $Z \leq 15$ for the reactions with the Al target) and at low velocities. As it extends to larger Z values for the reactions with the Al target than for the reactions with the Be target, it seems to be target related. In normal kinematics, this component corresponds to the high energy tail which is observed for atomic numbers near the projectile, and which is considered to be projectile related. Admittedly the origin of this component is not clear. While it is reminiscent of quasi-elastic and deep-inelastic

reactions, its extension to atomic numbers larger than the target is somewhat puzzling. Because of the large asymmetries of the entrance channels, one might expect a mass transfer in the opposite direction. Similarly, the possibility of a piece of the projectile being picked up promptly by the target is also dubious because the rather large excitation energy generated in the product should lead to its total disintegration. A way out of this quandary may be found in the motion of the nucleon clusters to be transferred inside the projectile. The clusters that are moving backwards in the center-of-mass of the projectile can be transferred without depositing much energy, thus allowing the resulting nucleus to survive complete disintegration.

Let us now return to the second component on which the present study focuses.

Even a cursory glance at the two ridges in the E-ΔE data shown in Figs. 3 & 4 conveys the idea of a fast moving single source emitting fragments more or less isotropically with a constant, sharp center-of-mass velocity. The two velocity components are readily understood as the two kinematic solutions expected at a small laboratory angle when a fast moving source decays into two fragments.

A more striking representation of these kinematics features is shown in Fig. 5b, which is a density plot of the invariant cross section $(\partial^2\sigma/\partial V_{\parallel}\partial V_{\perp})$ in the $V_{\parallel}$-$V_{\perp}$ plane for fragments with $11 \leq Z \leq 17$. Events from both detectors are included in this plot allowing a coverage of laboratory angles from 3° to 12°. Figure 5b shows clearly a portion of the Coulomb ring similar to the velocity diagram displayed in Fig. 5a. A portion of the ring is missing due to the limited angular coverage of the detectors. The width of the Coulomb ring is due to the inclusion of a range of fragment Z-values, each with their own Coulomb ring of a different radius, and to the spreading out of the individual fragment rings by sequential evaporation and Coulomb fluctuations.

From Fig. 5a, using simple geometric arguments one can show:

$$V_s = \frac{V_a + V_b}{2\cos\theta}. \qquad (2)$$

This suggests that the source velocity V_s can be obtained simply from the inclusive

velocity distributions. In practice, our detectors subtended a finite range of angles and the fragment velocity distributions have finite widths associated with them. A simulation incorporating these effects showed that the source velocity could be determined to less than 0.4% from

$$V_s = \frac{X_a + X_b}{2} , \qquad (3)$$

where X_a and X_b are the centroids of two gaussians fitted to the $V_{lab}/\cos\theta$ spectra.

Source velocities were derived for Z-species where the velocity spectra of the more forward angle detector (Detector 1) showed two, easily separated solutions and where the third, target-like component was not present. The experimental source velocities are shown in Fig. 8. The error bars on the experimental points indicate only the errors associated with the extraction procedure. The source velocities are rather independent of Z-value suggesting a common source for all of the fragments. This is similar to experimental source velocities obtained by Auger *et al.* [31]) for the reactions 35 MeV/u ^{84}Kr on ^{12}C and ^{27}Al. For the Kr + Al reaction, Auger *et al*. find that the source velocities display a small dependence on the fragment A-value. Their data suggest that for the more asymmetric mass splits, the associated mass transfers are on average larger. The source velocities for the Nb + Al reactions in this work, would not be inconsistent with an equivalent dependence on charge division.

The dotted lines in Fig. 8 represent the weighted mean of the experimental source velocities and the associated error bars represent the total systematic error from the energy calibration and mass parameterization. The source velocities give an indication on the degree of fusion in these reactions. The velocity corresponding to complete fusion is represented by the heavy dashed lines in Fig. 8. For an incomplete fusion reaction, the source velocity lies between this velocity and the beam velocity. The larger the source velocity, the less is the degree of fusion. The experimental source velocities indicate a high degree of fusion.

The average mass of the sources was estimated as

$$\langle A_s \rangle = A_p \frac{V_{beam}}{\langle V_s \rangle} \quad (4)$$

where A_p is the mass of the projectile and V_{beam} is the beam velocity. This equation was derived from momentum conservation, setting the momentum of the residual portion(s) of the target to zero. A more precise evaluation from the model of Ref. 1, leads to average masses which are within 2% of those obtained with this equation. The average source masses obtained from Equation 4, using the mean source velocities, are listed in Table 1. This table also lists the average total charge of the source $\langle Z_s \rangle$ assuming that the fraction of the target mass transferred is equal to the fraction of the target Z transferred.

The corresponding momentum transfers in normal kinematics, also listed in Table 1, are all consistent with the Viola systematics [32]) which predicts 68 to 76 % of full momentum transfer. However, for the reactions with the Be target, the data are not inconsistent with complete momentum transfer. It is difficult to measure accurately the degree of fusion in this reverse-kinematics reaction because the difference in source velocities between zero and full momentum transfer is small (≈9%).

The center-of-mass emission velocity of the fragments was obtained by an event-by-event transformation of the laboratory velocities into the frame associated with the average source velocity for each reaction. Figure 9 shows the first moment ($\langle V_e \rangle$) of the emission velocity distributions as a function of Z-value. In the same figure, the second moments are also presented; they will be discussed later. The results, for both targets, are very similar at the two bombarding energies. For comparison, the solid curves show a simple calculation where the emission velocities are derived solely from the Coulomb repulsion of the two fragments after scission. The scission configuration was assumed to be two spheres whose centers are separated by $1.2(A_1^{1/3}+A_2^{1/3})+2$ fm and where the Z split for each mass split is given by charge equilibration. This parameterization was found to reproduce emission velocities of complex fragments from compound nuclei at lower bombarding energies [24]).

At these higher excitation energies, it is important to include corrections due to the sequential evaporation of light particles from the primary fragments. To first order, sequential evaporation does not change the average velocity of a fragment, but it can

change the Z-value of the fragment. The estimation of the charge loss due to evaporation will be discussed later. The solid curves in Fig. 9 were calculated for the 25.4 MeV/u bombarding energy and include the effect of sequential evaporation. The calculations for the higher bombarding energy (not shown) are almost identical, as the corresponding sources were similar (Table 1). The agreement with the data is very good despite the fact that no angular momentum effects have been taken into account. In a way, this situation is very similar to that encountered for fully relaxed products in deep inelastic reactions, where Coulomb-like energies are always encountered despite large variations in the angular momentum. A partial compensation to an increase in angular momentum due to an increase in deformation is to be expected, but no quantitative verification of this effect is available as yet.

Coulomb velocities, calculated for symmetric division, using the Viola systematics of total fission kinetic energy [33]) are indicated in Fig. 9. These are also in excellent agreement with the experimental data.

3.2. ANGULAR DISTRIBUTIONS

The inclusive velocity spectra of complex fragments indicates that the fragments were emitted with Coulomb-like velocities in the binary division of intermediate systems formed in fusion-like reactions. This result is similar to those obtained at lower bombarding energies where complex fragments were characterized as decay products of compound nuclei produced in complete fusion reactions.

At these higher bombarding energies, it is of interest to establish whether the intermediate systems have attained complete relaxation and hence could be properly called compound nuclei. A necessary requirement for compound nucleus decay is the forward-backward symmetry of the angular distributions. One can test this forward-backward symmetry by comparing the yields of the high and low velocity kinematic solutions which correspond to emission forward and backward from the source system. The expected angular distribution for compound nuclear decay from a rapidly rotating system has approximately a $1/\sin\theta$ form in the frame of the source system.

Fig. 10 shows the ratio of the center-of-mass differential cross sections $d\sigma/d\theta$, obtained from the forward and backward kinematic solutions, as a function of fragment

Z-value. These ratios are consistent with a value of unity, and hence the yields are consistent with a $1/\sin\theta$ dependence of the angular distribution. This indicates a complete relaxation in the rotational degrees of freedom of the source.

3.3. CHARGE DISTRIBUTIONS AND CROSS SECTIONS

The ultimate test of compound nucleus decay can be made by comparing the experimental cross sections to the predictions of the statistical model. The essence of compound nucleus decay does not lie in the kinetic energy spectra or angular distributions of the product. Rather it is associated with the statistical competition between the decay channels. This automatically includes predictions for the kinetic energies and angular distributions. Consequently, it is in the absolute cross sections that one must search for the ultimate confirmation of the compound nucleus hypothesis.

The angle-integrated cross sections were obtained from the yields of the forward and backward solutions by assuming a $1/\sin\theta$ angular distribution. For fragments of low Z, where the third, target-like component was present, only the yields from the high energy solution were used as these are presumably free of contamination by this additional component. Angle-integrated cross sections for the target-like component could not be determined as its angular distribution is unknown. The cross sections, as a function of fragment Z-value, are shown in Fig. 11 together with the cross sections for the reaction 8.4 MeV/u Nb + Be from Ref. 24. The errors bars shown represent only the statistical error. The systematic error is estimated to be ±25%. There is very little difference in both the shape and magnitude of these cross sections between the 25.4 and 30.3 MeV/u bombarding energies for each target. However, there is a large increase in the cross sections as the bombarding energy is increased from 8.4 to 25.4 MeV/u for the Be target. The cross sections also show a large dependence on the target mass. The cross sections for the Al target are approximately a factor of 50 times larger than those for the Be target.

These cross sections are of course associated with the secondary fragments. The perturbation of the primary charge distributions by sequential evaporation is not expected to change their gross features. However, the finer structure which is visible, such as the systematic increase in C yields and decrease in F yields relative to the

general smooth trends, is probably associated with sequential evaporation.

The total cross sections summed over all binary divisions with $Z > 5$ represents approximately 1% of the total geometric cross section for the reactions with the Be target and 30% for the reactions with the Al target.

Cross sections have also been calculated with the statistical model using the transition state formalism for complex fragment emission. Following the approach of Moretto [22], one can calculate the decay width for binary division of the compound system into fragments Z_1,A_1 and Z_2,A_2 as

$$\Gamma(Z_1, A_1, Z_2, A_2) = \frac{1}{2\pi\, \rho(E^*\text{-}E_{rot}(J), J)} \int \rho^*(E^*\text{-}E_{sad}(J)\text{-}\varepsilon, J)\, d\varepsilon \qquad (5)$$

where ρ and ρ^* are the level densities of the compound nucleus and of the saddle-point configuration, respectively, $E_{rot}(J)$ and $E_{sad}(J)$ are the deformation plus rotational energies of the equilibrium and conditional saddle-point configurations, respectively. This expression can be approximated by

$$\Gamma(Z_1, A_1, Z_2, A_2) = \frac{T}{2\pi\, \rho(E^*\text{-}E_{rot}(J), J)}\, \rho^*(E^*\text{-}E_{sad}(J), J) \qquad (6)$$

where T is the temperature of the system at the conditional saddle-point configuration. In order to calculate Γ, one needs an estimate of the $E_{sad}(J)$. In the mass region of interest, the conditional saddle-points can be approximated by two nearly touching spheres. Thus, as a first approximation, the saddle-point energies were calculated as:

$$E_{sad} = E_{Coul} + Q_{ld}\,, \qquad (7)$$

where E_{Coul} is the Coulomb energy between the two spheres and Q_{ld} is the Q-value of the binary division calculated using liquid-drop masses. The separation between the surfaces of the spheres, chosen so as to reproduce the liquid-drop-model barriers for

symmetric division [34]), was approximately 2 fm for the systems of interest. Barriers calculated in this manner reproduce asymmetric liquid-drop barriers for ^{110}In as calculated by Sierk [26]). The angular momentum dependence was included using the rigid body moment-of-inertia of the saddle-point configuration, which gives excellent agreement with the Rotating Liquid-Drop-Model barriers [35]) except at the largest angular momenta. These "liquid-drop" barriers are, however, expected to be too large as they neglect the nuclear force between the the two nascent fragments. A full treatment of the conditional saddle-points configurations has been made by Sierk [26]) for the system ^{110}In using the Finite-Range Model which incorporates finite range surface-surface interactions. As finite-range barriers were unavailable for the nuclei under consideration, approximate values were obtained by scaling the "liquid-drop" barriers in such a way as to reproduce the symmetric finite-range barriers [36]). However for ^{110}In, the barriers obtained by this procedure, for the very asymmetric splits, are still larger than the corresponding finite-range barriers calculated by Sierk. For $Z \approx 5$ fragments, the difference is about 5 MeV. It is estimated, that for the asymmetric divisions, the yields calculated with the scaled liquid-drop barriers may be up to a factor of 3 smaller than the corresponding yields that would be calculated with finite-range barriers.

For the large excitation energies associated with these reactions, multi-chance emission of complex fragments can be an important effect. The evaporation code PACE was used to calculate the the E^*,J populations of intermediate systems produced in the decay of the compound nucleus by light particle evaporation. The complex fragment cross sections from the compound nucleus and each of these intermediate systems were calculated using the decay widths of Equation 6 and the total decay width calculated by PACE. All binary decays which give rise to primary fragments contained in the nuclear mass table of Wapstra and Bos [37]) were allowed in the statistical model calculations. No depletion in the populations of sequential intermediate systems due to complex fragment emission was considered. This may result in an over estimation of the cross sections for the reactions with the Al target by up to a factor of 2. However, the effect is much smaller for the reactions with the Be target.

As a starting point is these calculations, one needs to know the initial Z, A, E*, J distributions of the compound systems produced in the incomplete fusion reactions.

For lack of any experimental guidance in estimating these distributions, the simple abrasion model of Ref. 1, which was discussed in the introduction, was employed. The dependence of the excitation energy and transferred angular momentum upon the entrance channel L-wave predicted is illustrated in Fig.12 for the 30.3 MeV/u Nb + Be reaction. In the model, complete fusion occurs for all impact parameters below a critical value. For L-waves above this value the non-occluded portion of the target is sheared off and there is a sharp drop in both the transferred angular momentum and the excitation energy of the fusion-like product. This results in a sharp drop in the complex fragment decay probability. However, incomplete fusion products can contribute significantly to the total complex fragment yields due to their larger geometric cross sections. This is illustrated in Fig.13, where calculated cross sections for Z=20 fragments are shown as a function of the entrance channel L-wave. For the Nb + Be reaction, most of the yield is predicted to be produced by L-waves which result in complete fusion. The sharp drop in the complex fragment decay probability due to the onset of incomplete fusion is clearly seen. However for the reactions with the Al target, the calculations suggest that the total yield is dominated by the incomplete fusion component; after the onset of incomplete fusion the cross section drops rapidly, but quickly rises again due to the increasing geometrical cross sections of the larger L-waves.

In Table 2, the experimental source velocities are compared to the predictions of these calculations. For all reactions, the predicted source velocities are smaller than the experimental quantities. Better agreement with experiment source velocities may be achieved by incorporating the prompt emission of light particles (Fermi jets) [38,39,7]) into the incomplete fusion model. This would result in a decrease in the momentum transfer even for the central collisions. It would also reduce the excitation energy of the fusion-like products. However, this may not have a great effect on the predicted cross sections. Figure 14 shows the predicted complex fragment decay probability as a function of E^* and J. For the Nb + Al reactions, most of the complex fragment yield is predicted to be produced by fusion-like products with angular momenta from 50 to 60 $\hbar$. For such J values, the predicted complex fragment yield becomes flat with increasing excitation energy. Complete fusion results in 610 MeV and 490 MeV of excitation energy for 30.3 MeV/u and 25.4 MeV/u reactions with the Al target,

respectively. A large amount of excitation energy could be lost by Fermi jet processes and not change the decay probability. However, if such processes remove significant amounts of angular momentum, this effect would decrease the decay probability substantially.

The calculated complex fragment cross sections are compared to the experimental data in Fig.11. In view of the many assumptions associated with these calculations and the simplicity of the incomplete fusion model, the calculated cross sections are in excellent agreement with experiment. In spite of the many uncertainties, the calculations account quantitatively for the large differences in the complex fragment cross sections between the reactions with the Be and Al targets, and also for the large increase in cross sections relative to the 8.4 MeV/u data. The conclusion of this analysis provides the most powerful argument in favor of the compound nucleus hypothesis, namely the fact that the cross sections are consistent with the compound nucleus branching ratios.

3.4. EXCITATION ENERGIES

The data suggest the formation of a hot equilibrated compound system in an incomplete fusion reaction. Following the assumptions used to calculate the source mass, the average excitation energy of the compound systems is given by

$$\langle E_s^* \rangle = \frac{\langle A_s \rangle - A_p}{\langle A_s \rangle} E_{beam} + \langle Q \rangle \ , \qquad (8)$$

where <Q> is the average Q-value for the various possible exist channels associated with the experimental mass transfer. In this work, the Q-values used were -5.4 MeV for the reactions with the Be target and -30 MeV for the reactions with the Al target. The derived excitation energies are listed in Table 1. These excitation energies are remarkably large. At their highest values, they are a sizable fraction of the total nuclear binding energies. The corresponding temperatures, on the one hand, are approaching the binding energy per nucleon, and on the other hand, are a good fraction of the Fermi energies. These compound nuclei are indeed much hotter than those typically found at lower bombarding energies, and one may wonder if their behavior deviates in

any way from that observed at the lower energies.

The present technique could be extended to higher bombarding energies in order to verify the range of existence of compound nuclei and to search for new processes that may occur above the limit of compound nucleus stability. The same technique, when used in conjunction with light particle coincidences, can lead to valuable information on the evolution of compound nucleus properties with excitation energy. Typical effects one would be looking for are changes in the Coulomb barriers and variations in branching ratios due to the rapid changes of the relevant thermodynamic functions as one approaches the critical point from below.

3.5. VELOCITY FLUCTUATIONS

The compound systems formed in these reactions decay largely via light particle evaporation leading to the formation of evaporation residues. However, a fraction of the nuclei undergo binary division forming complex fragments. These fragments are emitted with Coulomb velocities. The second moment of the primary fragment V_e distributions are due to the fluctuations in the Coulomb energy at the scission point arising from fluctuations in various bound collective degrees of freedom.

Following the formalism of Moretto [22]), the width associated with this effect is approximately

$$\sigma_{Coul} = \sqrt{\frac{(p_1 + p_2)\, T}{2} + (n+1)\, T^2}\ , \qquad (9)$$

where p_1 and p_2 are amplifying parameters associated with the spheroidal oscillation of each nascent fragment, n is the number of non-amplifying modes, and T is the temperature of the system at the saddle-scission point. Amplifying factors were derived from a two-spheroid liquid-drop model. They were calculated for a saddle-point configuration with angular momentum of 30 and 50 $\hbar$ for the reactions with the Be and Al targets, respectively. However, the dependence of the calculated amplifying factors on the angular momentum is not large. (An increase of the angular momentum by 10 $\hbar$ results in an increase of $\approx$ 10% in the amplifying factors.) The widths derived from

these amplifying factors, using n=1 and temperatures obtained from the excitation energies in Table 1, are shown in Fig. 9 (curve "1") for 25.4 MeV/u reactions.

The emission velocity of the primary fragments is perturbed by the sequential evaporation of light particles. The contribution of this effect to experimental V_e distributions was estimated by means of the evaporation code PACE. The excitation energy of the primary fragments E^*_f was calculated from the following formula which assumes equal temperatures of the two fragments after scission:

$$E^*_f = \frac{A_f}{A_s} (E^*_s + Q_{ld} - E_{Coul}) \quad . \tag{10}$$

Here A_f is the atomic mass of the primary fragment, A_s and E^*_s are the atomic mass and excitation energy of the composite system from Table 1 and Q_{ld} and E_{Coul} are the same quantities as in Eq.7. The width due to sequential evaporation was calculated from the R.M.S recoil velocity V_{recoil} predicted by PACE, as

$$\sigma_{evap} = \frac{V_{recoil}}{\sqrt{3}} \, . \tag{11}$$

The results of the calculation of σ_{evap} are shown in Fig.9 as curve"2". Curve "3" shows the width due to the range of primary fragment Z-values associated with each secondary Z-value. The magnitude of this component was estimated from the PACE simulations. The resultant total moment obtained from the three components added in quadrature is indicated by the curve "T" in the figure.

For the 25.4 MeV/u Nb + Be reactions, these moments account for most of the experimentally determined quantities. However, for the 25.4 MeV/u Nb +Al reaction, the calculated moments are significantly smaller than the experimental data. This may reflect the uncertainties associated with these calculations or may be due to the effect of pre-scission evaporation and/or to a distribution of source velocities, both of which could contribute to the experimental widths.

4. Coincidence data.

4.1 Z_1-Z_2 CORRELATIONS

The binary character of complex fragment emission, clearly visible in the velocity spectra, is also seen in the coincidence measurements. Figure 15 shows the Z_1 - Z_2 correlation of coincidence events where Z_1 and Z_2 are the atomic charges of the particles recorded in detector 1 and 2, respectively. Most of the events lie in bands corresponding to an approximate constant sum of Z_1 and Z_2. This can be seen more clearly in Fig. 16, where the spectra of $Z_1 + Z_2$ are shown. For comparison, the solid curve in Fig. 15 and the arrows in Fig. 16 correspond to a value of $Z_1 + Z_2$ equal to the average atomic number of the source listed in Table 1. Of course, one should not expect to observe the total Z of the incomplete-fusion product because of the inevitable sequential evaporation from the hot primary fragments. One can check the internal consistency of our picture by calculating the secondary charge loss due to evaporation. This was done with the evaporation code PACE. The results are shown in Fig. 15, where the range of the products expected from sequential evaporation are indicated by the hatched regions. The widths of these regions correspond to approximately ±3 standard deviations of the predicted secondary charge distribution associated with each primary fragment. These regions enclose a large fraction of the experimental data. The population of the hatched regions by the experimental data is weighted towards asymmetric divisions where the heavier fragment is detected in Detector 1 and the lighter fragment is detector in Detector 2. The more favorable selection of these events over the other possibilities is trivially due to the asymmetric placement of the detectors about the beam axis. For the reactions with the Al target, the few events to the left of the binary bands could be due to higher multiplicity decays. However, they amount to no more than 5% of the total number of coincidence events (see Fig. 16).

Even more illuminating is Fig. 17, where the average sum of the charges $\langle Z_1 + Z_2 \rangle$ is plotted versus Z_2. The dashed lines indicate the average charge of the source estimated from the experimental source velocity. The solid curves indicate the calculated residual charge after sequential evaporation. This was obtained by subtracting the average charge loss predicted by PACE for each mass split from the

average source charge. These calculated values of $\langle Z_1 + Z_2 \rangle$ are not too sensitive to the exact amount of momentum transfer. A smaller momentum transfer implies a larger charge loss in the incomplete fusion process. This is balanced, to a large degree, by a reduction in the charge removed by sequential evaporation due to the decrease in the excitation energy of the primary fragments. The uncertainty associated with the extracted momentum transfer gives rise to a change in the calculated values of $\langle Z_1 + Z_2 \rangle$ of only ± 1.5 Z-units for all reactions. In Fig. 17, the agreement between the calculations and the data is quite good, despite the broad range of excitation energies covered by our reactions and the associated range of charge losses, which is 2-4 Z units for the ^{9}Be target and 13 - 15 Z-units for the ^{27}Al targets.

The significance of this agreement is in the consistency of the following sequence of inferences: 1) source velocity $\rightarrow$ mass transfer $\rightarrow$ excitation energy $\rightarrow$ secondary charge loss. The question remains as to whether the charge loss occurs before or after the binary decay. While the previous calculations assumed that the secondary decay occurred after complex fragment emission, the predicted residual charge is not very sensitive to a sizable amount of pre-scission evaporation.

4.2 COINCIDENCE EFFICIENCY

The coincidence efficiency (ratio of coincidence yield to the inclusive yield) for Detector 1 is plotted in Fig. 18 as a function of the fragment Z-value. Despite the modest sizes of the detectors, these efficiencies are reasonably large (10 - 20%) for a range of charge divisions. This is due to the strong kinematic focusing in reverse-kinematics reactions.

The coincidence efficiency has also been evaluated with a Monte Carlo simulation of binary decay followed by sequential evaporation. In the simulation, the fragments are emitted from a system travelling along the beam axis with the experimental source velocity. The fragments are emitted with Coulomb velocities which included the effect of the fluctuations in the Coulomb energy. The net effect of the sequential evaporation of light particles is assumed to result in a recoil velocity distribution which is isotropic and has a gaussian form along each of the three principal directions. This simulation incorporated our detector geometry and included the effects of the finite beam spot size as well as the divergence of the beam at the target. The results of the simulation are

show by the solid curves in Fig. 18. They are in reasonable agreement with the experimental data. This means that essentially all the inclusive events are accounted for by the coincidence events. In other words, essentially all the observed inclusive events are physical binary events. The extra coincidence yield for $Z_1 < 20$ in the Nb + Al reactions is due to the higher multiplicity decays; an inspection of Fig. 15 clearly shows that there are very few binary events in this region.

5. Conclusions

The present work demonstrates, that in these very asymmetric reactions, compound nucleus emission represents the main source of complex fragments with Z-values greater that the target Z-value and it is also an important source for the lighter fragments. Such compound nuclei are produced in fusion-like reactions with very large excitation energies. Complex fragment emission is a very powerful tool for the study of extremely hot compound nuclei at the limit of their existence.

This work was supported by the Director, Office of Energy Research, Division of Nuclear Physics of the Office of High Energy and Nuclear Physics of the U. S. Department of Energy under Contract DE-AC03-76SF00098.

Table 1. The average atomic number, atomic charge, excitation energy, excitation energy per nucleon, and temperature of the source and the linear momentum transfer extracted for the reactions of this work. Both the statistical and systematic error (in parentheses) are presented for each of these quantities .

E/A (MeV)	25.4	30.3	25.4	30.3
Target	^{9}Be	^{9}Be	^{27}Al	^{27}Al
$\langle p/p_{beam} \rangle$ in normal kin.	0.64±0.10 (±0.20)	0.70±0.10 (±0.20)	0.73±0.05 (±0.10)	0.65±0.05 (±0.10)
$\langle A_S \rangle$	98.8±1.0(±2.0)	99.4±1.0(±2.0)	112.9±1.3(±2.6)	110.6±1.3(±2.6)
$\langle Z_S \rangle$	43.6±0.5(±1.0)	43.8±0.5(±1.0)	50.5±0.6(±1.4)	49.5±0.6(±1.4)
$\langle E^* \rangle$ (MeV)	134±20(±40)	175±25(±50)	385±25(±50)	418±30(±60)
$\langle E^*/A \rangle$ (MeV)	1.4±0.2(±0.4)	1.9±0.2(±0.5)	3.4±0.2(±0.5)	3.7±0.2(±0.5)
$\langle T \rangle$ [t] (MeV)	3.3±0.2(±0.4)	3.7±0.2(±0.4)	5.2±0.2(±0.3)	5.5±0.2(±0.4)

[t] $a = A/8\ MeV^{-1}$

Table 2. Experimental and calculated source velocities as a ratio of the complete fusion velocity. Both the statistical and systematic error (in parentheses) are presented for the experimental results.

E/A(^{93}Nb) (MeV)	Target	V_s/V_{cf} Experiment	V_s/V_{cf} Calculated
25.4	Be	1.03±0.01(±0.02)	1.00
30.3	Be	1.03±0.01(±0.02)	1.00
25.4	Al	1.06±0.01(±0.02)	1.03
30.3	Al	1.09±0.01(±0.02)	1.05

References

1) L.G. Moretto and D.R. Bowman, XXIV International Winter Meeting on Nuclear Physics, Bormio 1986, Ricerca Scientifica ed Educazione Permanente, suppl. 49, 1986, p. 126, Ed . I. Iori.

2) G.D. Westfall, J. Gosset, P.J. Johansen, A.M. Poskanzer, W.G. Meyer, H.H. Gutbrod, A. Sandoval, and R. Stock, Phys. Rev. Lett. **37** (1976)1202.

3) D. Jacquet, E. Duek, J.M. Alexander, B. Borderie, J. Galin, D. Gardes, D. Guerreau, M. Lefort, F. Monnet, M.F. Rivet, and X. Tarrago, Phys. Rev. Lett. **53** (1984) 2226.

4) M. Conjeaud, S. Harar, M. Mostefai, E.C. Pollacco, C. Volant, Y. Cassagnou, R. Dayras, R. Legrain, H. Oeschler, and F. Saint-Laurent, Phys. Lett. **159B** (1985) 244.

5) M. Fatyga, K. Kwiatkowski, V.E. Viola, C.B. Chitwood, D.J. Fields, C.K. Gelbke, W.G. Lynch, J. Pochodzalla, M.B. Tsang, and M. Blann, Phys. Rev. Lett. **55** (1985)1376.

6) H. Morgenstern, W. Bohne, W. Galster, K. Grabisch, and A. Kyanowski, Phys. Rev. Lett. **52** (1984) 1104.

7) G.S.F. Stephans, D.G. Kovar, R.V.F. Janssens, G. Rosner, H. Ikezoe, B. Wilkins, D. Henderson, K.T. Lesko, J.J. Kolata, C.K. Gelbke, B.V. Jacak, Z.M. Koenig, G.D. Westfall, A. Szanto de Toledo, E.M. Szanto, and P.L. Gonthier, Phys. Lett. **161B** (1985) 60.

8) G. Auger, D. Jouan, E. Plagnol, F. Pougheon, F. Naulin, H. Doubre, and C. Grégoire, Z. Phys. **A321** (1985) 243.

9) A. M. Poskanzer, G.W. Butler, and E.K. Hyde, Phys. Rev. **C3** (1971) 882.

10) E.K. Hyde, G.W. Butler, and A.M. Poskanzer, Phys. Rev. **C4** (1971) 1759.

11) J.E. Finn, S. Agarwal, A. Bujak, J. Chuang, L.J. Gutay, A.S. Hirsch, R.W. Minich, N.T. Porile, R.P. Scharenberg, B. C. Stringfellow, and F. Turkot, Phys. Rev. Lett. **49** (1982) 1321.

12) C.B. Chitwood, D.J. Fields, C.K. Gelbke, W.G. Lynch, A.D. Panagiotou, M.B. Tsang, H. Utsunomiya, and W.A. Friedman, Phys. Lett. **131B** (1983) 289.

13) A.S. Hirsch, A. Bujak, J.E. Finn, L.J. Gutay, R.W. Minich, N.T. Porile, R.P. Scharenberg, B.C. Stringfellow, and F. Turkot, Phys. Rev. **C29** (1984) 508.

14) R. Trockel, K.D. Hildenbrand, U. Lynen, W.F.J. Mueller, H.J. Rabe, H. Sann, H. Stelzer, R. Wada, N. Brummund, R. Glasow, K.H. Kampert, R. Santo, D. Pelte, J. Pochodzalla, and E. Eckert, Gesellschaft für Schwerionenforschung preprint GSI-85-45 (1985).

15) D.J. Fields, W.G. Lynch, T.K. Nayak, M.B. Tsang, C.B. Chitwood, C.K. Gelbke, R. Morse, J. Wilczynski, T.C. Awes, R.L. Ferguson, F. Plasil, F.E. Obenshain, and G [illegible]oung, Phys. Rev. **C34** (1986) 536.

16) A.D. Panagiotou, M.W. Curtin, and D.K. Scott, Phys. Rev. **C31** (1985) 55.

17) M. E. Fisher, Physics **3** (1967) 255.

18) G. Fái and J. Randrup, Nucl. Phys. **A381** (1982) 557.

19) J.P. Bondorf, R. Donangelo, I.N. Mishustin, C.J. Pethick, H. Schulz, and K. Sneppen, Nucl. Phys. **A443** (1985) 321.

20) H.W. Barz, J.P. Bondorf, R. Donangelo, I.N. Mishustin, and H. Schulz, Nucl. Phys. **A448** (1986) 753.

21) J. Aichelin, J. Hüfner, and R. Ibarra, Phys. Rev. **C30** (1984) 107.

22) L.G. Moretto, Nucl. Phys. **A247** (1975) 211.

23) L.G. Sobotka, M.L. Padgett, G.J. Wozniak, G. Guarino, A.J. Pacheco, L.G. Moretto, Y. Chan, R.G. Stokstad, I. Tserruya, and S. Wald, Phys. Rev. Lett. **51** (1983) 2187.

24) L.G. Sobotka, M.A. McMahan, R.J. McDonald, C. Signarbieux, G.J. Wozniak, M.L. Padgett, J.H. Gu, Z.H. Liu, Z.Q. Yao, and L.G. Moretto, Phys. Rev. Lett. **53** (1984) 2004.

25) M.A. McMahan, L.G. Moretto, M.L. Padgett, G.J. Wozniak, L.G. Sobotka, and M.G. Mustafa, Phys. Rev. Lett. **54** (1985) 1995.

26) A.J. Sierk, Phys. Rev. Lett. **55** (1985) 582.

27) R.J. Charity, M.A. McMahan, D.R. Bowman, Z.H. Liu, R.J. McDonald, G.J. Wozniak, L.G. Moretto, S. Bradley, W.L. Kehoe, A.C. Mignerey, and M.N. Namboodiri, Phys. Rev. Lett. **56** (1986) 1354.

28) F. Hubert, A. Fleury, R. Bimbot, and D. Gardes, Ann. Phys. (Fr.) **5** (1980) Suppl.

29) J.B. Moulton, J.E Stephenson, R.P. Schmitt, and G.J. Wozniak, Nucl. Instr. & Meth. **157** (1978) 325.

30) A. Gavron, Phys. Rev. **C21** (1980) 230.

31) F. Auger, B. Berthier, A. Cunsolo, A. Foti, W. Mittig, J.M. Pascaud, E. Plagnol, J. Québert, and J.P. Wieleczko, Phys. Rev. **C35** (1987) 190.

32) V.E. Viola, Jr., B.B. Back, K.L. Wolf, T.C. Awes, C.K. Gelbke, H. Breuer, Phys. Rev. **C26** (1982) 178.

33) V.E. Viola, K. Kwiatkowski, and M. Walker, Phys. Rev. **C31** (1985) 1550.

34) S. Cohen and W.J. Swiatecki, Ann. Phys. **22** (1963) 406.

35) S. Cohen, F. Plasil and W.J. Swiatecki, Ann. Phys. **82** (1974) 557.

36) H.J Krappe, J.R. Nix, and A.J. Sierk, Phys. Rev. **C20** (1979) 992.

37) A.H. Wapstra and K. Bos, Atom. Data Nucl. Data Tabl. **19** (1977) 177.

38) C. Grégoire and F. Scheuter, Phys. Lett. **146B** (1984) 21.

39) C. Ngô and S. Leray, Z. Phys. **A322** (1985) 419.

Figure Captions

Fig. 1. The predicted impact parameters, as a function of bombarding energy, at which it is possible to shear-off part of the target or projectile in the reaction Nb + Be (calculated from Ref.1).

Fig. 2. Schematic plot of how the mass distribution of complex fragments emitted from a compound nucleus (A≈100) varies with the excitation energy of the compound nucleus. Mass distributions are shown here for a light compound nucleus which has a minimum in the yield for symmetric division. As the excitation energy increases, the yield dramatically increases and the distributions become flatter.

Fig. 3. Density plot of E-ΔE for the reaction 25.4 MeV/u Nb on Be for particles detected from 3^o to 8^o.

Fig. 4. Density plot of E-ΔE for the reaction 30.3 MeV/u Nb on Al for particles detected from 3^o to 8^o.

Fig. 5. a) Schematic representation of the kinematics for compound-nucleus fragment emission in reverse-kinematics. b) Density plot of the invariant cross section ($\partial^2\sigma/\partial V_{\parallel}\partial V_{\perp}$) in the $V_{\parallel}$-$V_{\perp}$ plane for fragments of $11 \leq Z \leq 17$ for the reaction 30.3 MeV/u Nb on Be.

Fig. 6. Contours of the invariant cross section in the Z- velocity plane. Data below the dashed curves for the Be targets correspond to events where the fragments did not stop in the E detector.

Fig. 7. Evaporation-residue angular distribution for the reaction 25.4 MeV/u Nb on Be as calculated with the code PACE.

Fig. 8. Source velocities extracted from the inclusive data as a function of the fragment Z-value. The error bars associated with the experimental points show only the uncertainty of the extraction procedure (see text). The dotted lines shows the weighted mean of the experimental data. The error bars associated with these lines represent the total systematic error.

Fig. 9. Extracted first and second moments of the center-of-mass emission velocity distributions of complex fragments plotted as a function of the fragment Z-value for both the Nb + Be and Al reactions at 25.4 and 30.3 MeV/u. The solid curves shows the results of a simple calculation of Coulomb velocities (see text). Emission velocities for symmetric division calculated from the Viola systematics [33]) are indicated. Curves 1, 2, & 3 represent the estimated widths associated with: 1) fluctuations in the Coulomb energy; 2) sequential evaporation from the primary fragments; and 3) the range of primary Z-values associated with each secondary Z-value. Curve "T" shows the total width from these three components added in quadrature.

Fig. 10. Ratios of $d\sigma/d\theta$ for the high and low velocity kinematic solutions as a function of the fragment Z-value. A ratio of unity corresponds to a $1/\sin\theta$ distribution in $d\sigma/d\Omega$.

Fig. 11. Angle-integrated cross sections (extracted from this work and Ref. 24) plotted as a function of the fragment Z-value. These data are compared to statistical model calculations shown by the solid curves.

Fig. 12. The excitation energy of the compound system produced in the fusion-like reaction plotted as a function of the transferred angular momentum of compound nuclei predicted by the geometric incomplete fusion model of Ref. 1 for 30.3 MeV/u Nb on Be reaction. The entrance channel L-waves corresponding to various regions of E^* and J are indicated.

Fig. 13. Calculated cross sections for Z=20 complex fragments produced in the reactions 25.4 MeV/u Nb on Be & Al targets, plotted as a function of entrance channel L-wave.

Fig. 14. Predicted probability of emitting a Z=20 fragment in the decay of the compound nucleus ^{120}Xe as a function of excitation energy. The curves correspond to different transferred angular momenta.

Fig. 15. Scatter plots of the experimental Z_1-Z_2 correlation for coincidence fragments. The solid lines correspond to the estimated total charge of the source systems given in Table 1. The shaded area represents an estimate of the regions where binary events should lie following sequential evaporation from the primary fragments (see text).

Fig.16. The relative yield of coincidence events plotted as a function of the sum of the atomic charges of the two coincident fragments. The arrows correspond to an estimation of the initial Z-value of the compound nucleus produced in each reaction.

Fig. 17. The mean sum, $\langle Z_1+Z_2 \rangle$ of coincidence events plotted as a function of the fragment atomic number in Detector 2. The dashed lines indicate the average charge of the source system estimated from the mass transfer. The charge loss for binary events due to sequential evaporation was estimated using the evaporation code PACE, and the residual $Z_1 + Z_2$ values are indicated by the solid curves.

Fig. 18. The coincidence efficiency (ratio of the coincidence yield to the inclusive yield) measured in Detector 1 plotted as a function of the fragment Z-value in Detector 1. The solid curves show the results of a Monte Carlo simulation (see text).

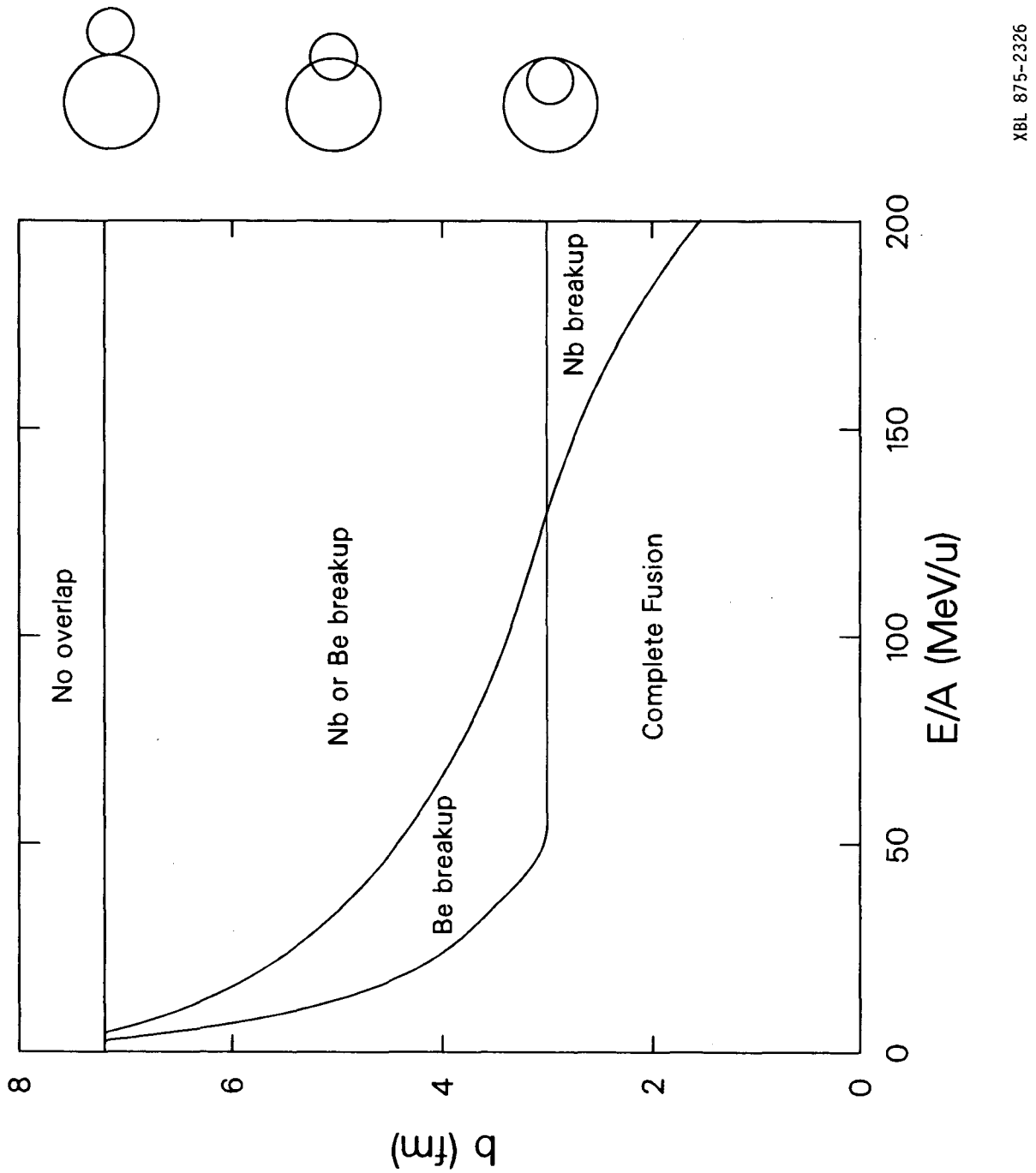
No overlap
Nb or Be breakup
Be breakup
Nb breakup
Complete Fusion
b (fm)
E/A (MeV/u)
0
2
4
6
8
0
50
100
150
200
XBL 875-2326

Fig. 1

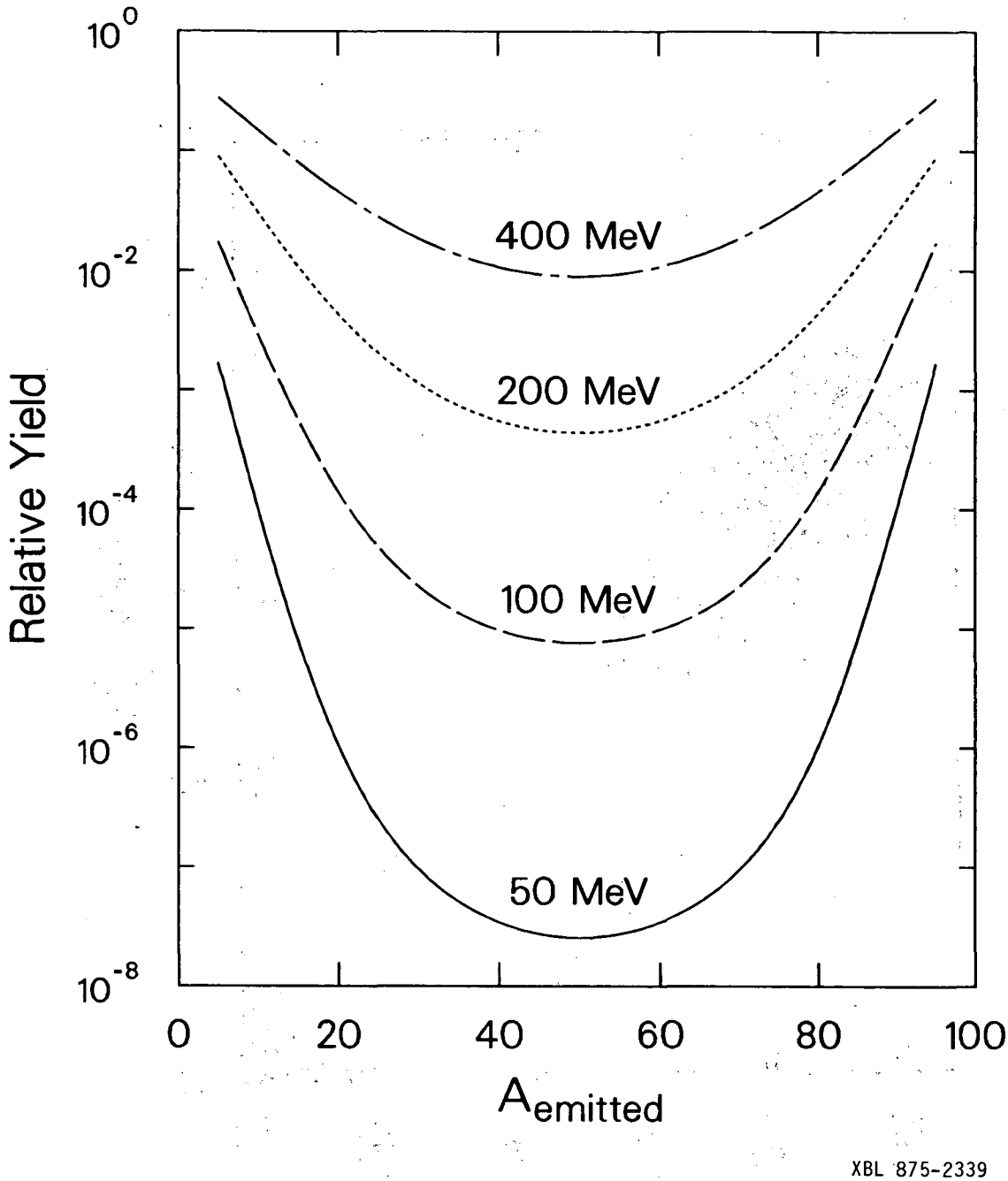
10^0
10^{-2}
10^{-4}
10^{-6}
10^{-8}
Relative Yield
400 MeV
200 MeV
100 MeV
50 MeV
0
20
40
60
80
100
$A_{emitted}$
XBL 875-2339

Fig. 2

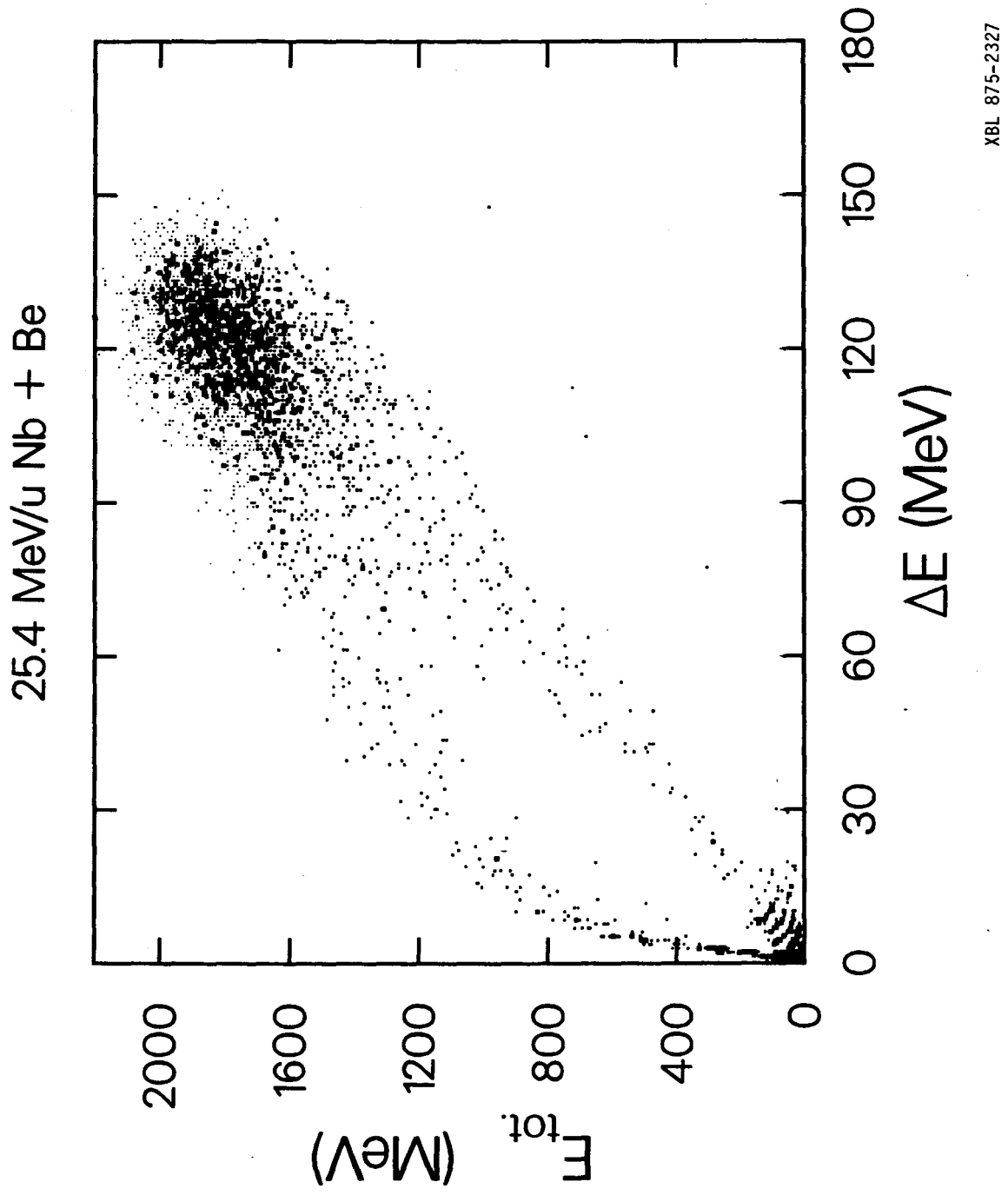
25.4 MeV/u Nb + Be
$E_{tot.}$ (MeV)
2000
1600
1200
800
400
0
0
30
60
90
120
150
180
ΔE (MeV)
XBL 875-2327

Fig. 3

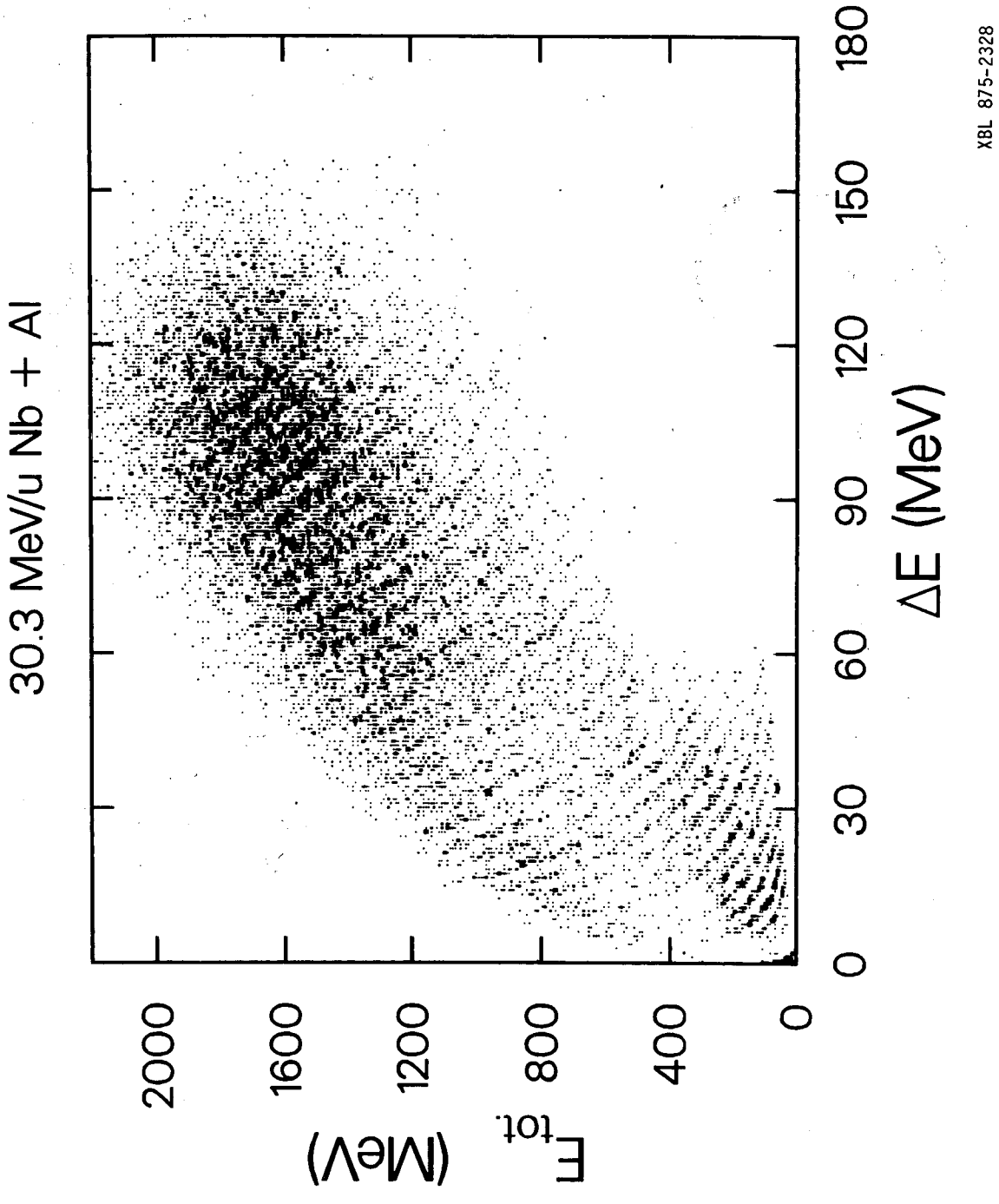
30.3 MeV/u Nb + Al
$E_{tot.}$ (MeV)
2000
1600
1200
800
400
0
0
30
60
90
120
150
180
ΔE (MeV)
XBL 875-2328

Fig. 4

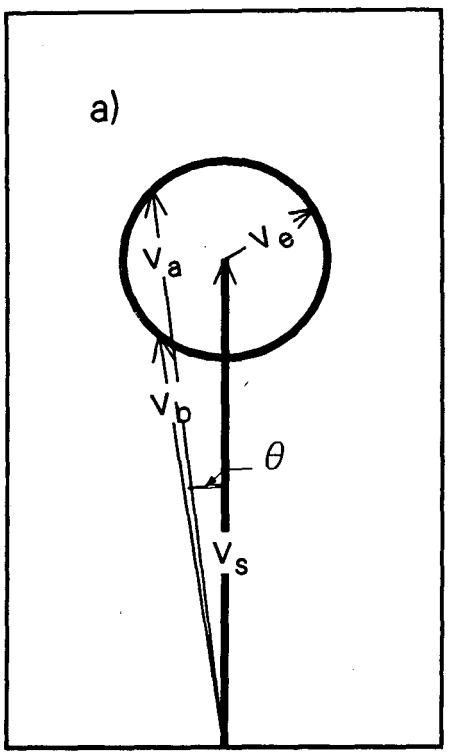

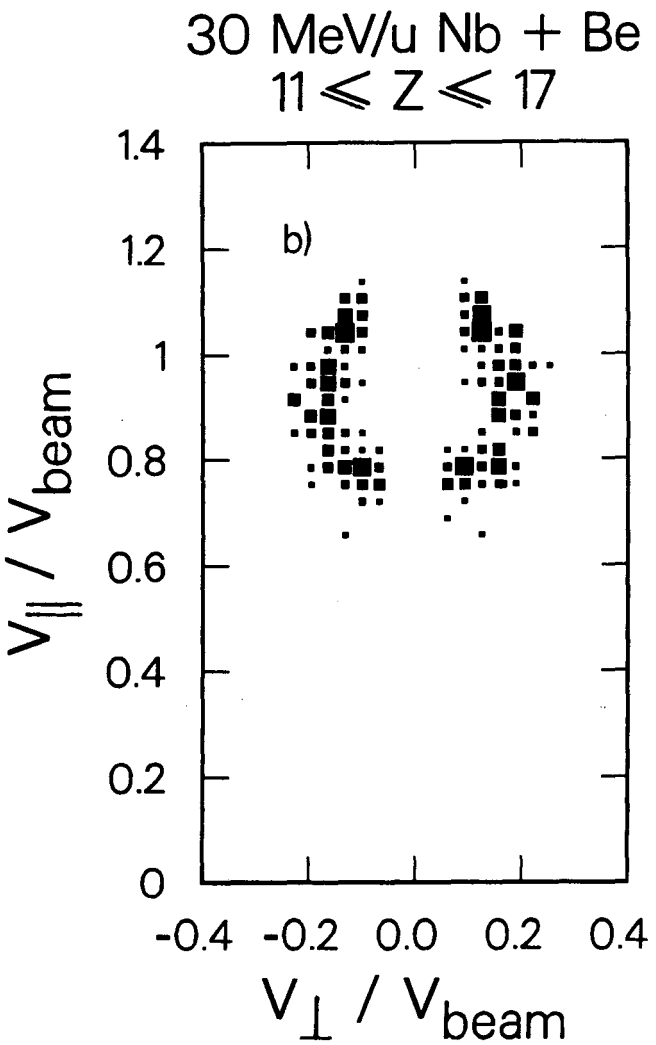

XBL 875-2329

Fig. 5

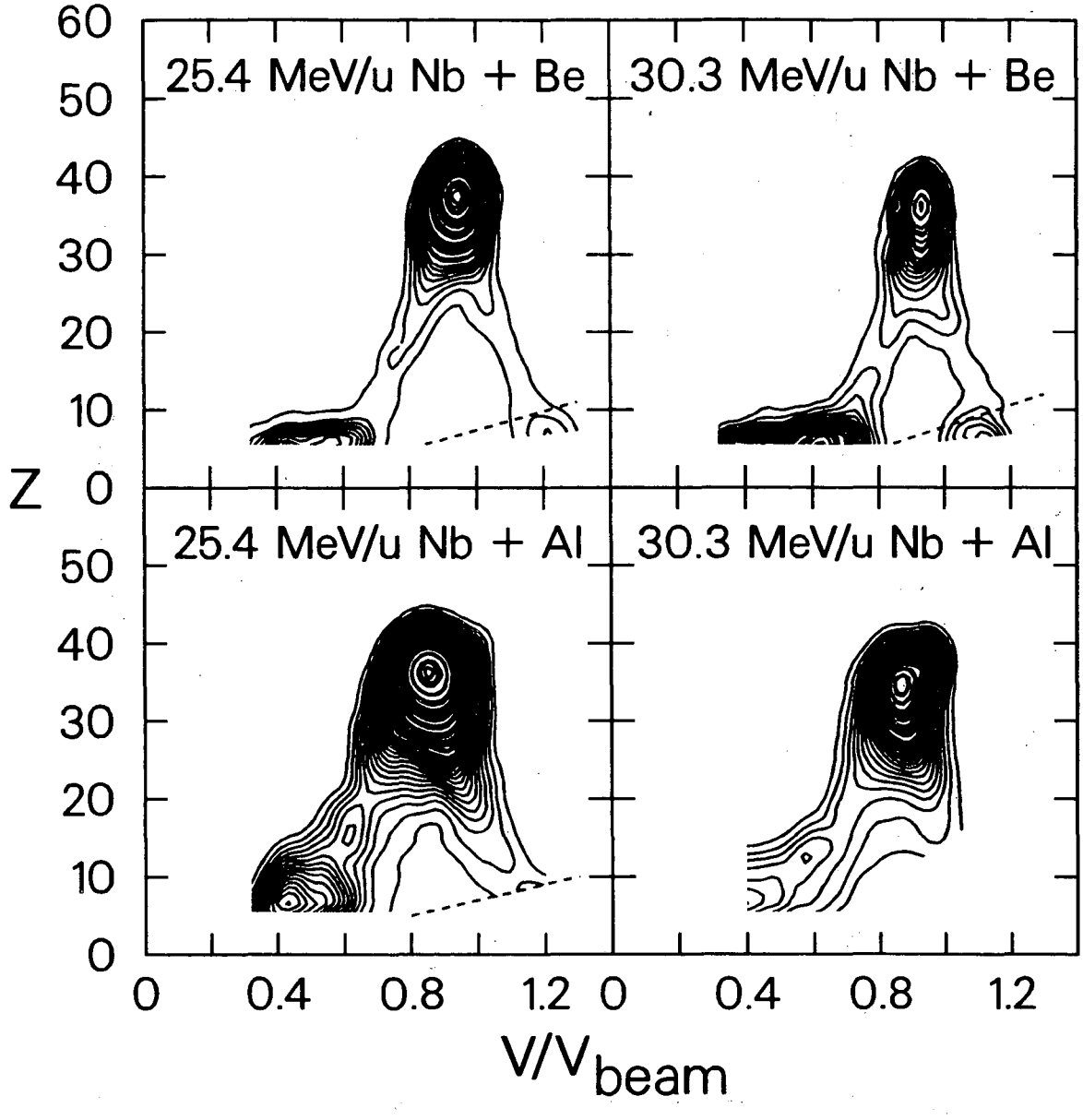

XBL 875-2340

Fig. 6

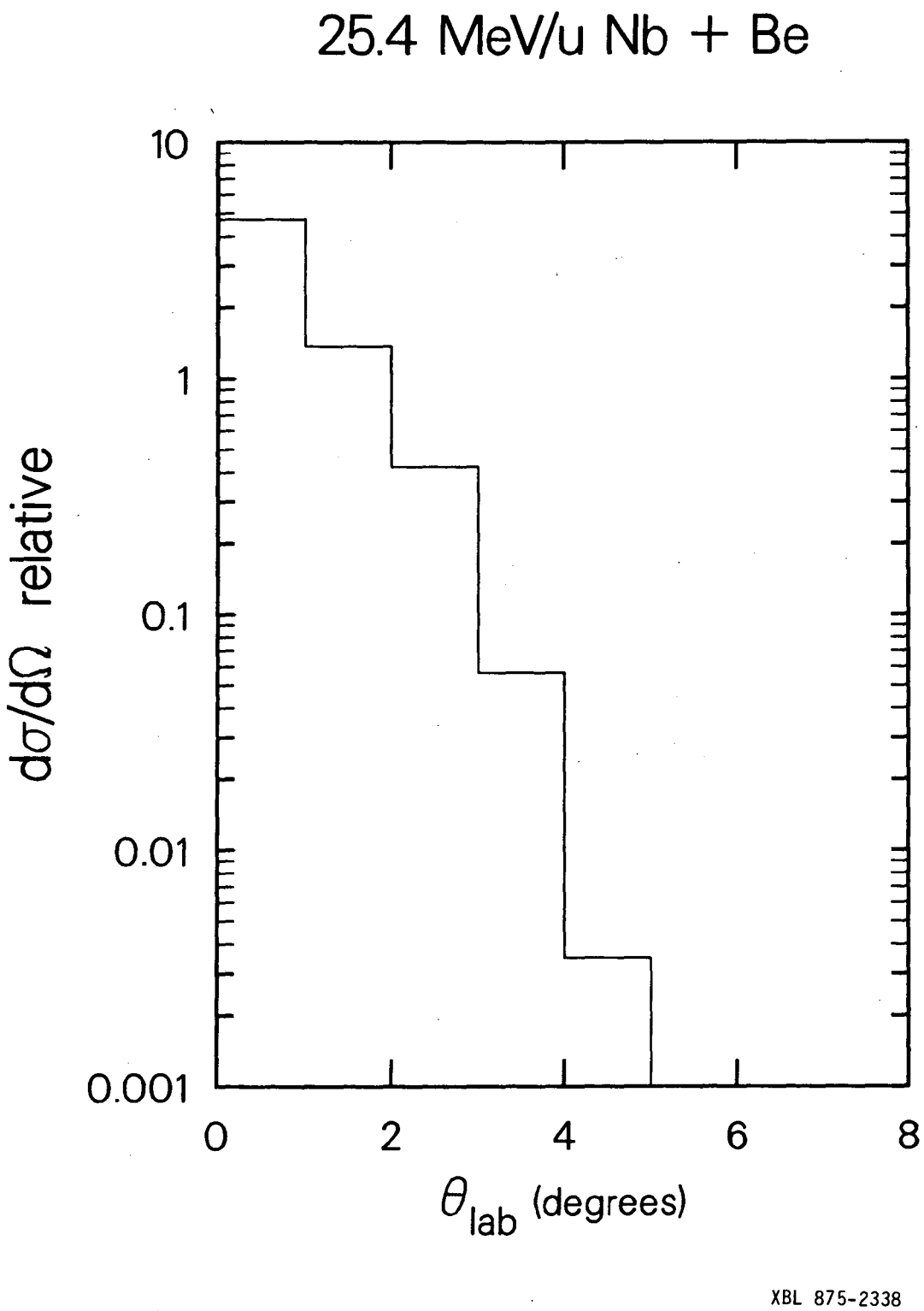
25.4 MeV/u Nb + Be
10
1
0.1
0.01
0.001
dσ/dΩ relative
0
2
4
6
8
θlab (degrees)
XBL 875-2338

Fig. 7

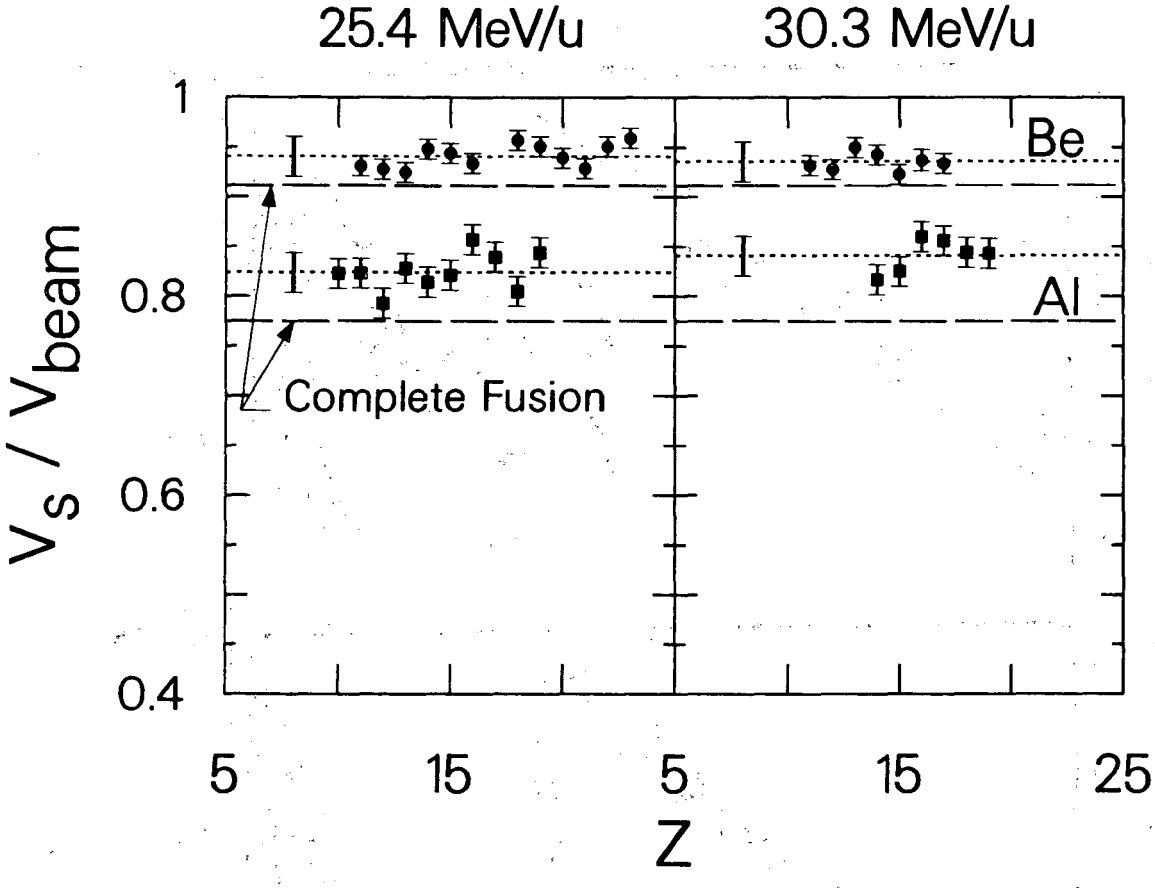
25.4 MeV/u
30.3 MeV/u
1
0.8
0.6
0.4
V_s / V_{beam}
Be
Al
Complete Fusion
5
15
5
15
25
Z
XBL 875-2337

Fig. 8

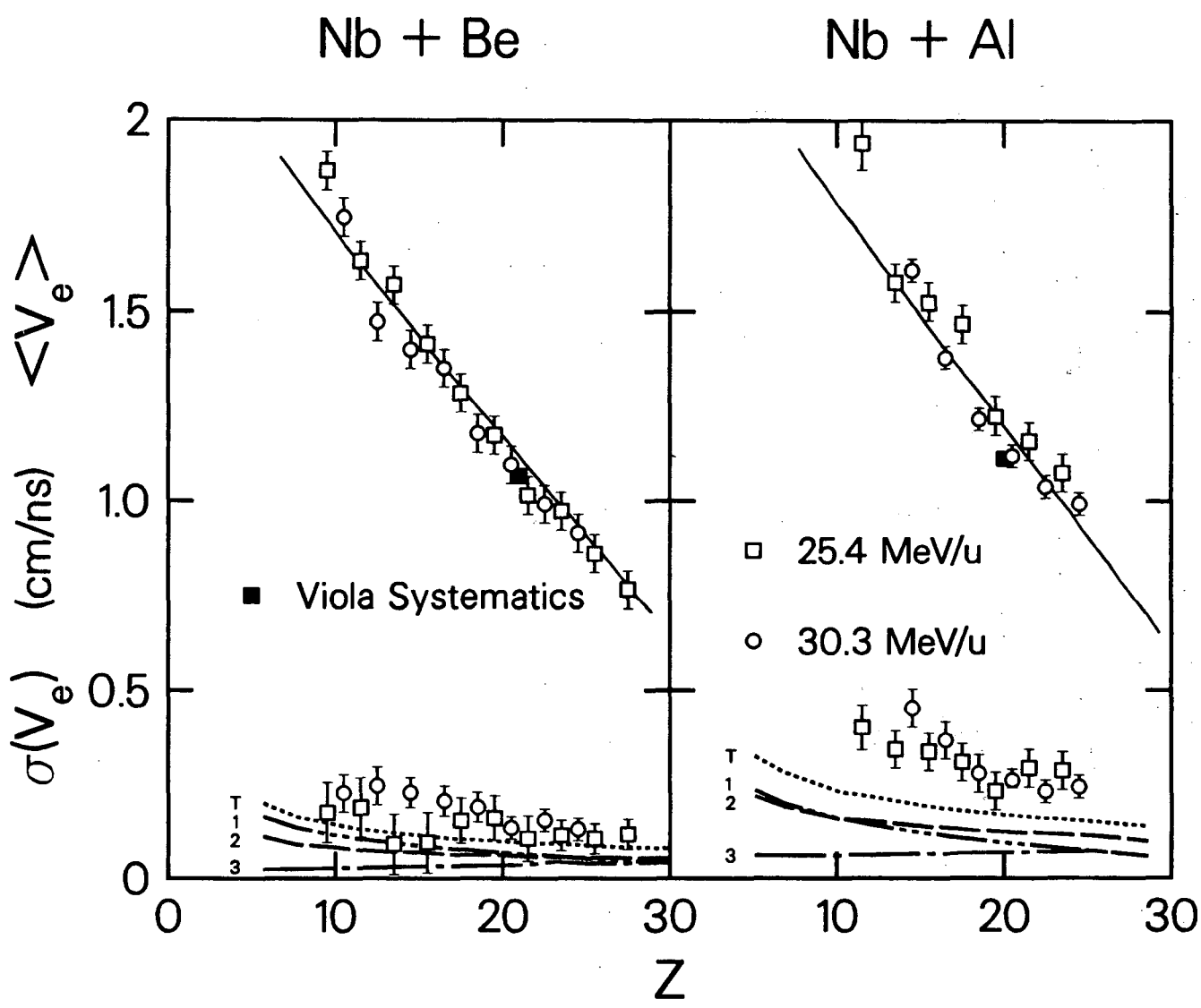
Nb + Be
Nb + Al
2
1.5
1.0
0.5
0
$\sigma(V_e)$ (cm/ns) $\langle V_e \rangle$
Viola Systematics
25.4 MeV/u
30.3 MeV/u
T
1
2
3
0
10
20
30
Z
XBL 875-2330

Fig. 9

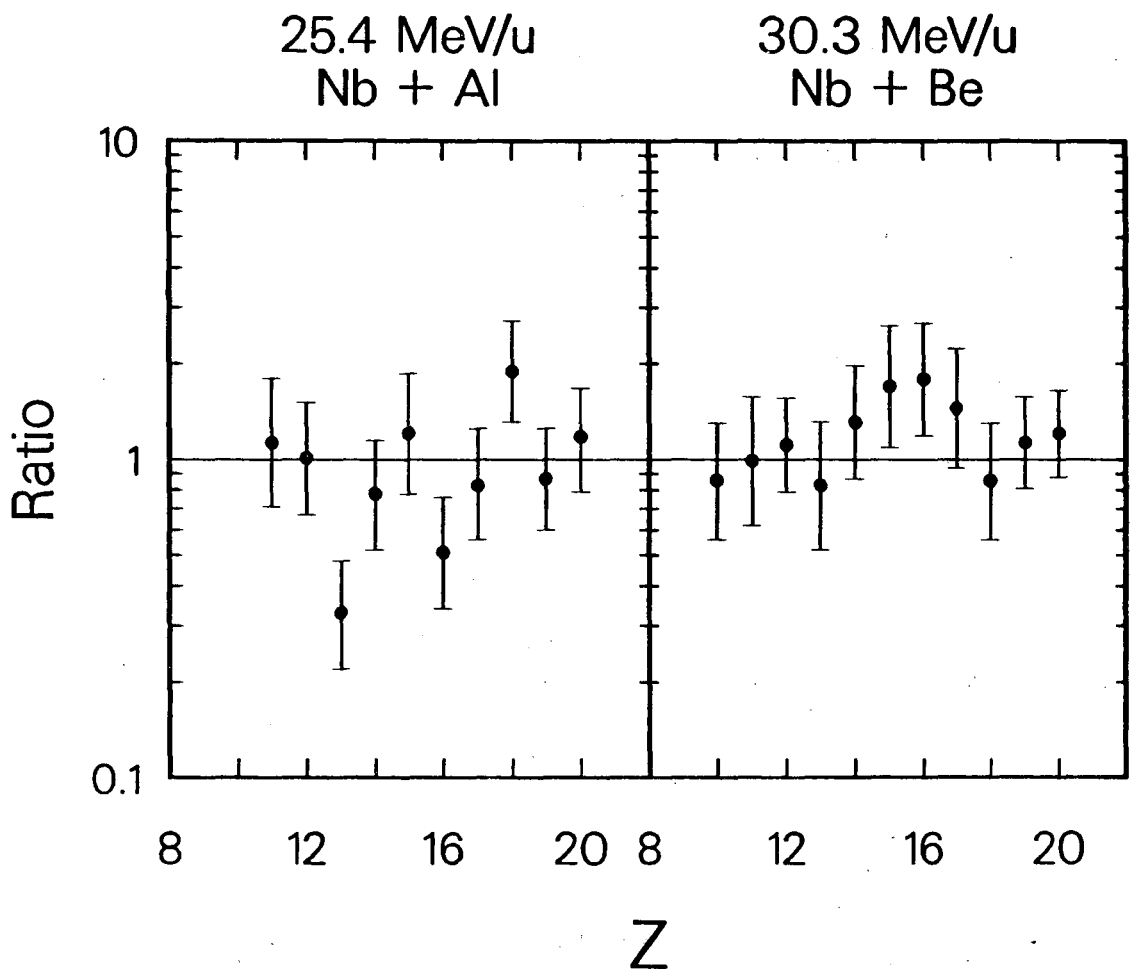

XBL 873-1333

Fig. 10

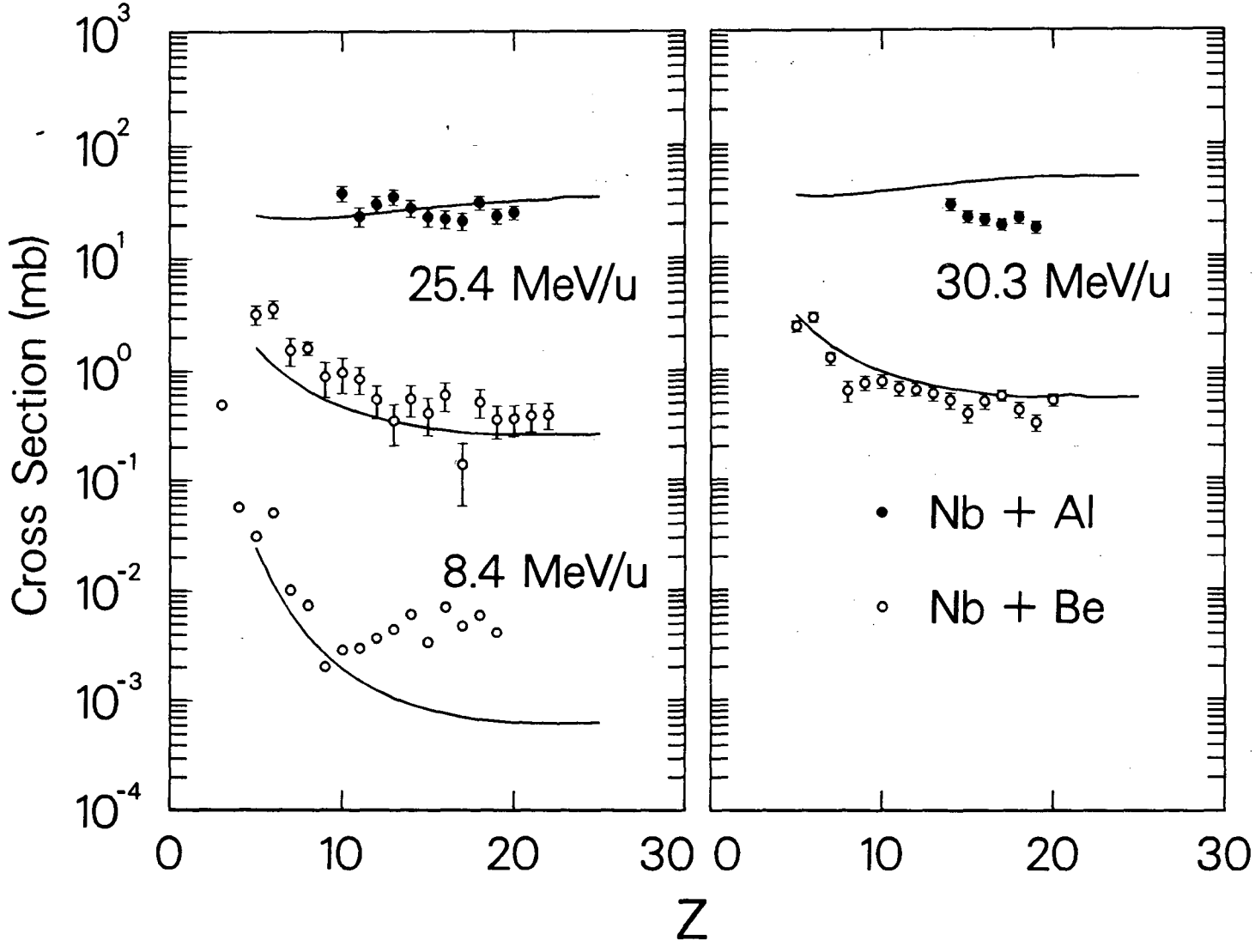

XBL 875-2331

Fig. 11

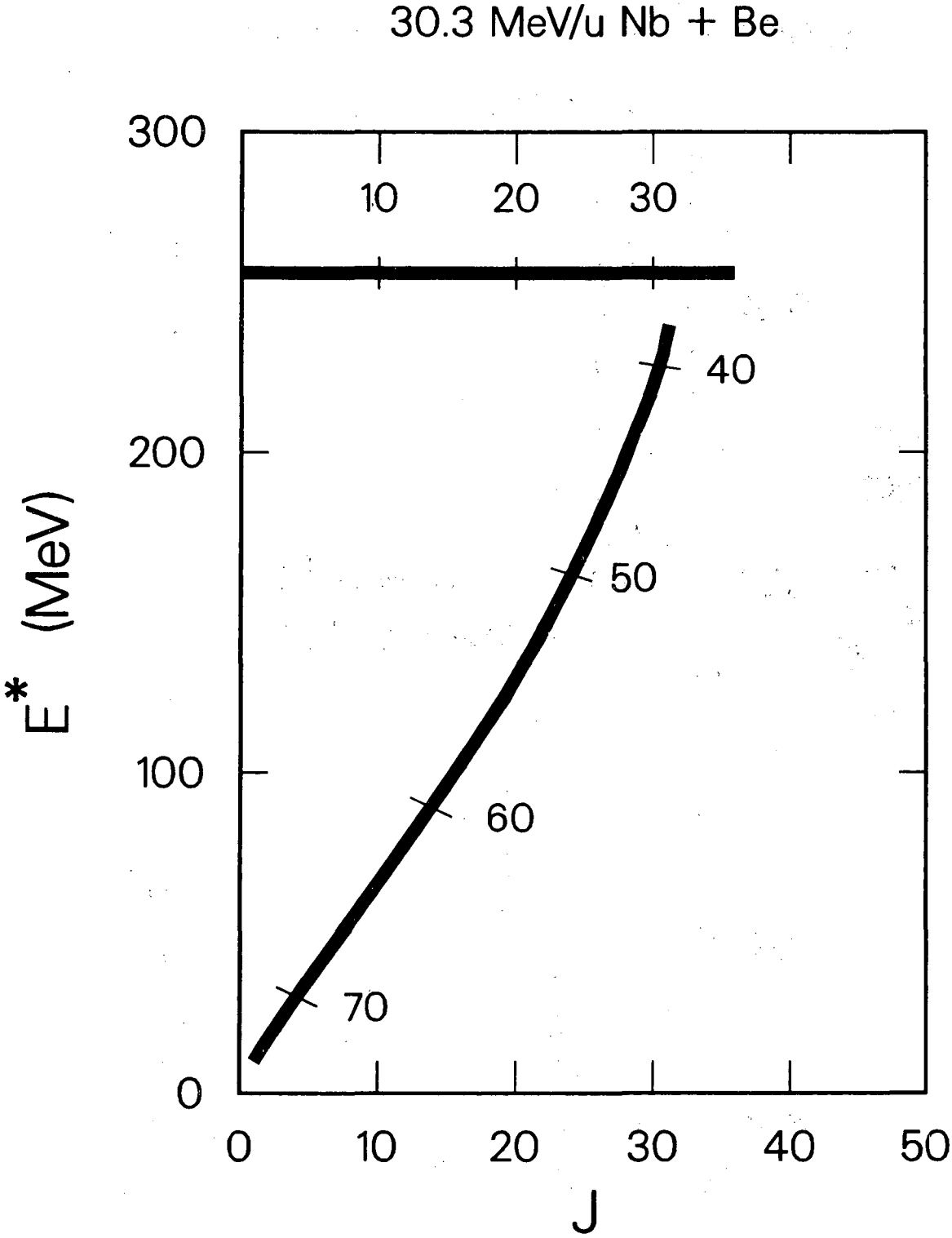
30.3 MeV/u Nb + Be
300
200
100
0
E* (MeV)
10
20
30
40
50
60
70
0
10
20
30
40
50
J
XBL 875-2336

Fig. 12

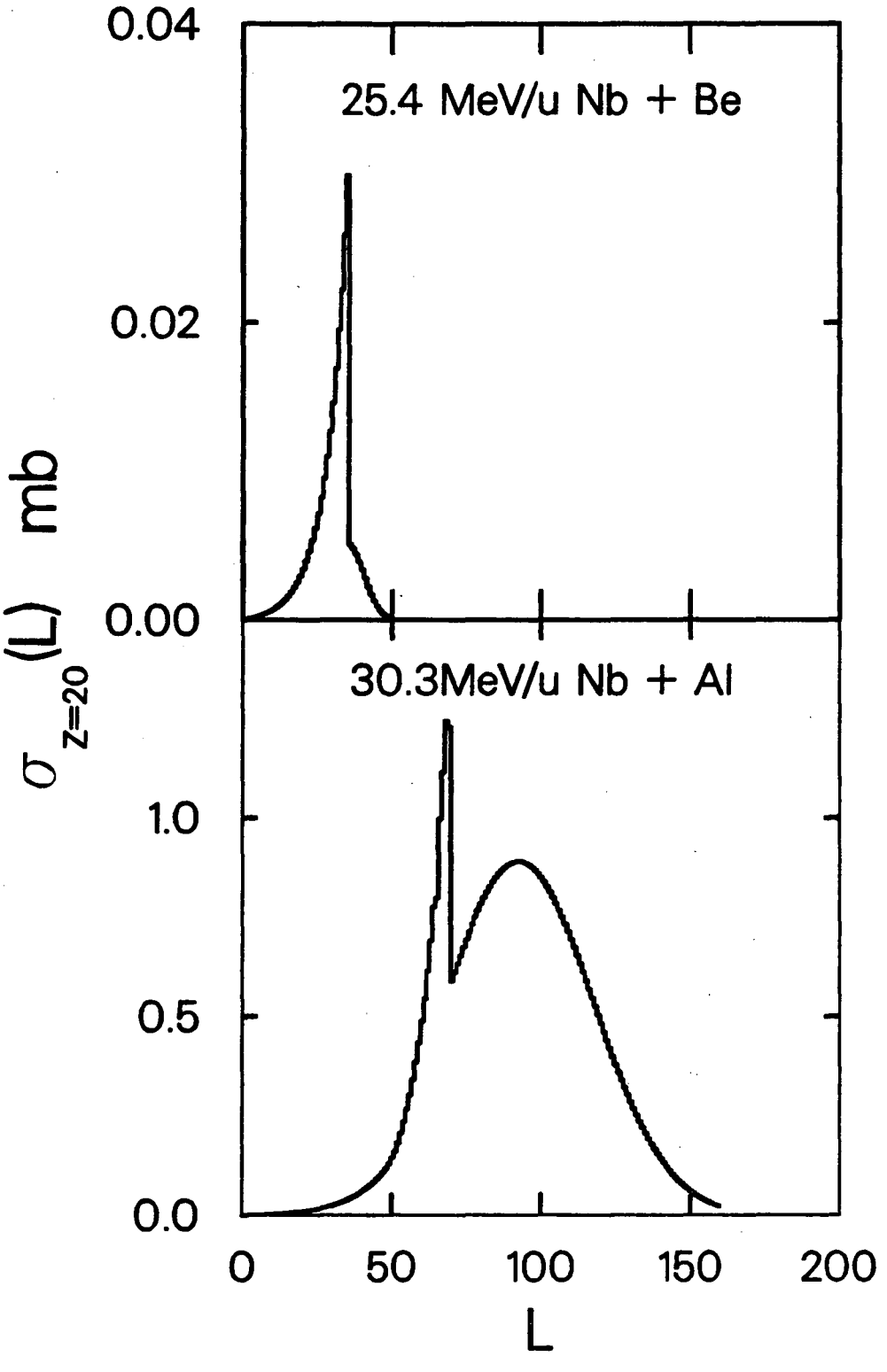
0.04
0.02
0.00
25.4 MeV/u Nb + Be
30.3MeV/u Nb + Al
1.0
0.5
0.0
$\sigma_{z=20}(L)$ mb
0
50
100
150
200
L
XBL 873-1335

Fig. 13

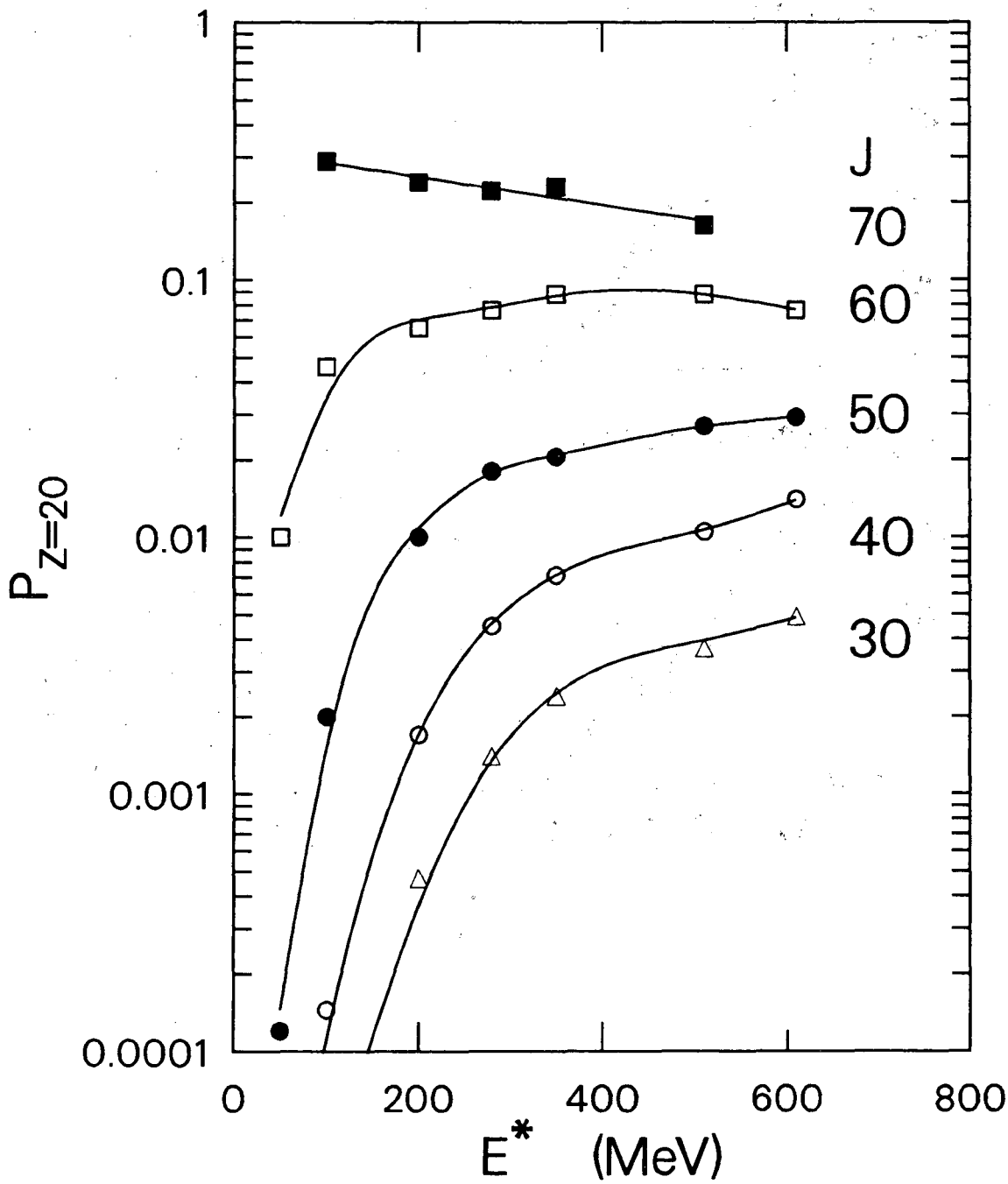
Z=54 A=120
1
0.1
0.01
0.001
0.0001
$P_{Z=20}$
0
200
400
600
800
E^* (MeV)
J
70
60
50
40
30
XBL 875-2333

Fig. 14

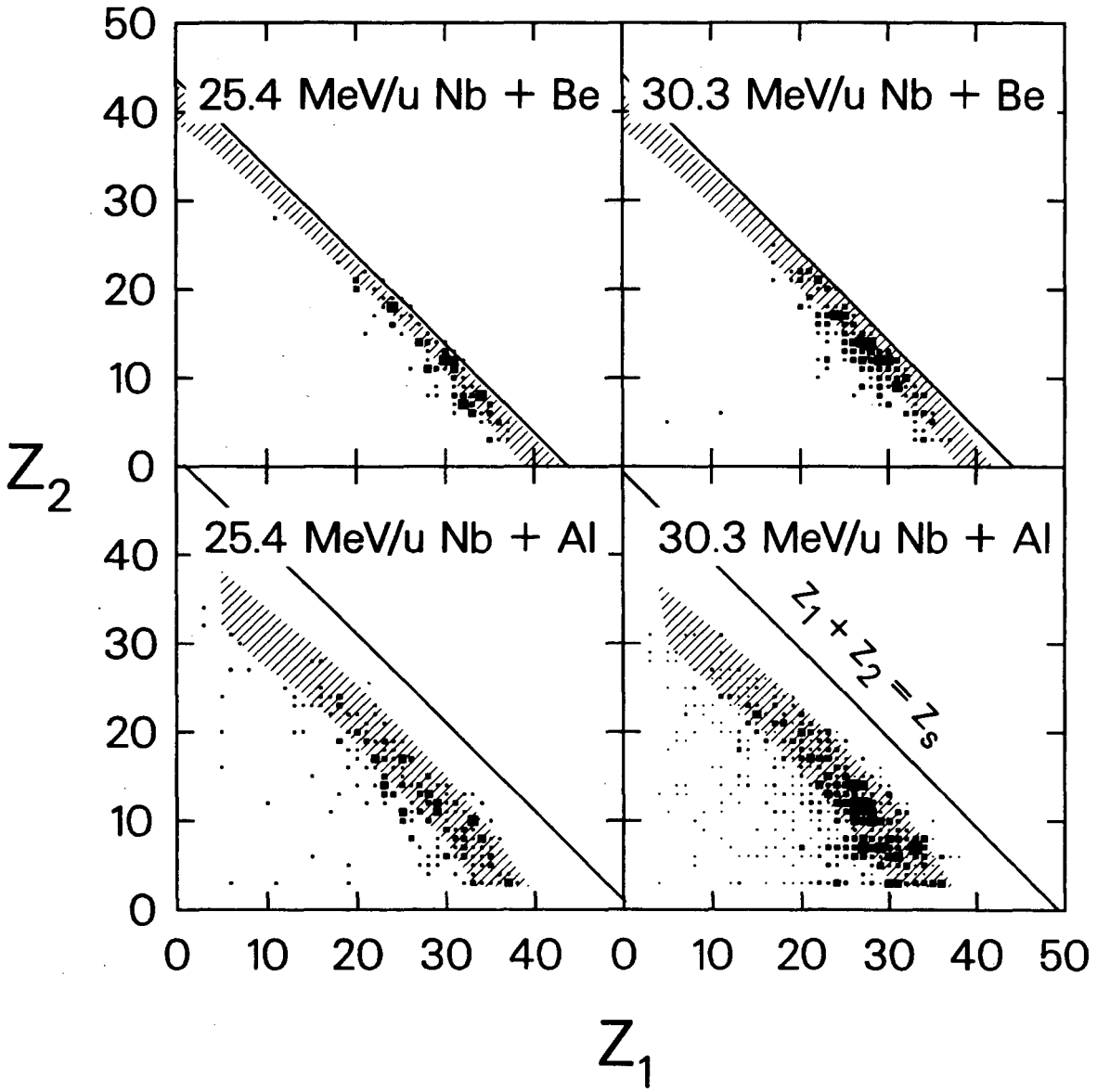

XBL 875-2335

Fig. 15

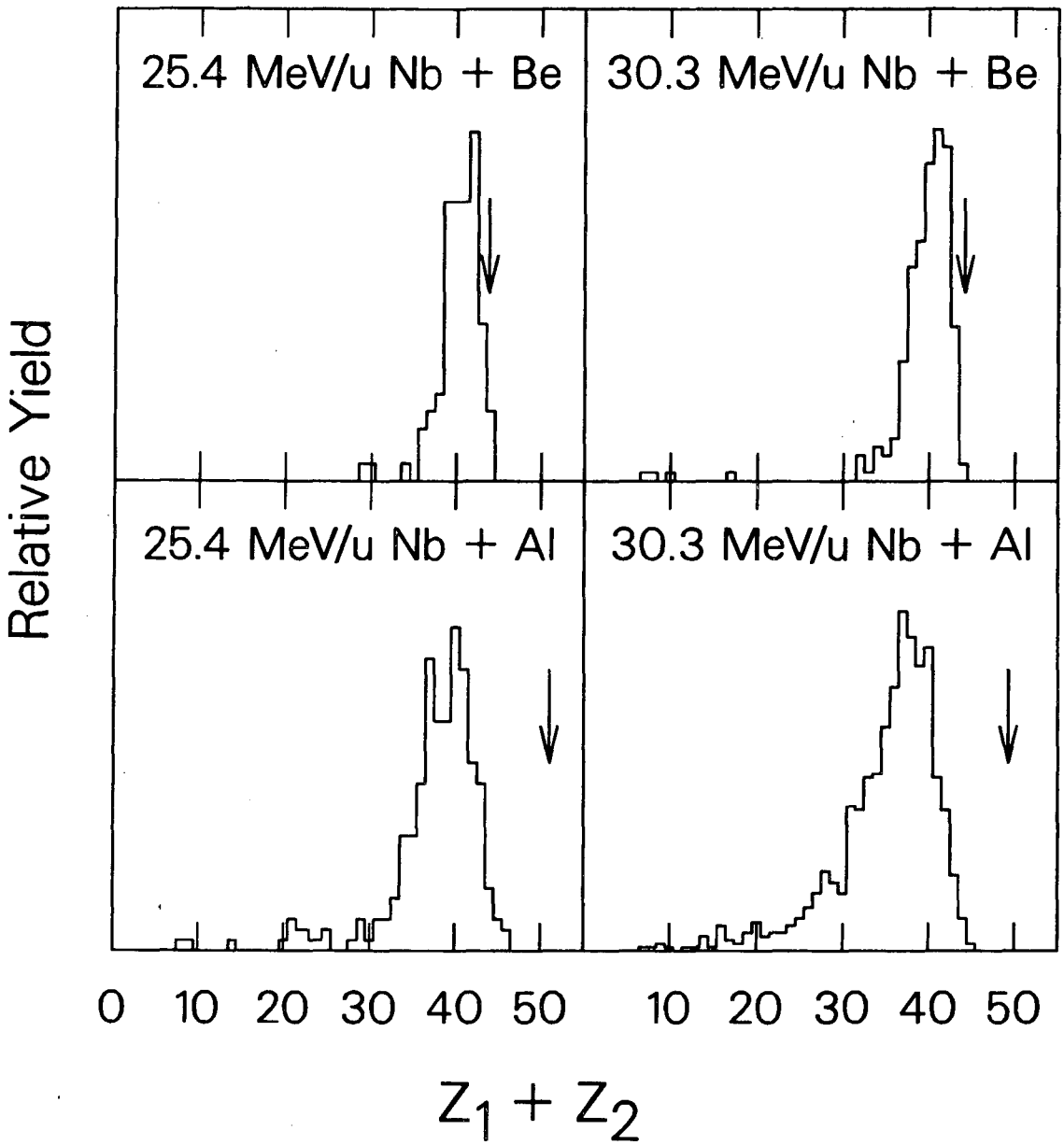

XBL 875-2334

Fig. 16

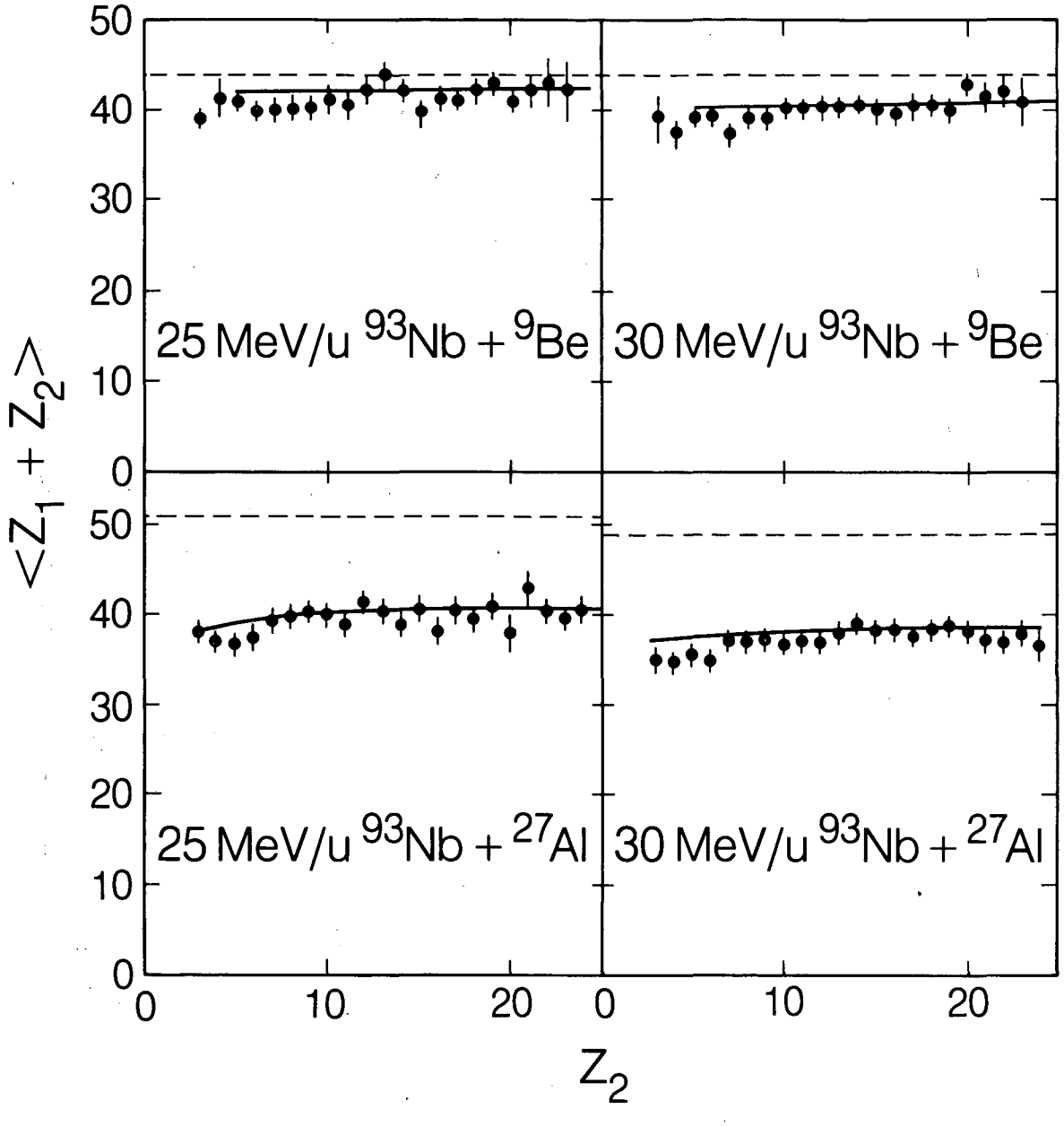

XBL 859-8977

Fig. 17

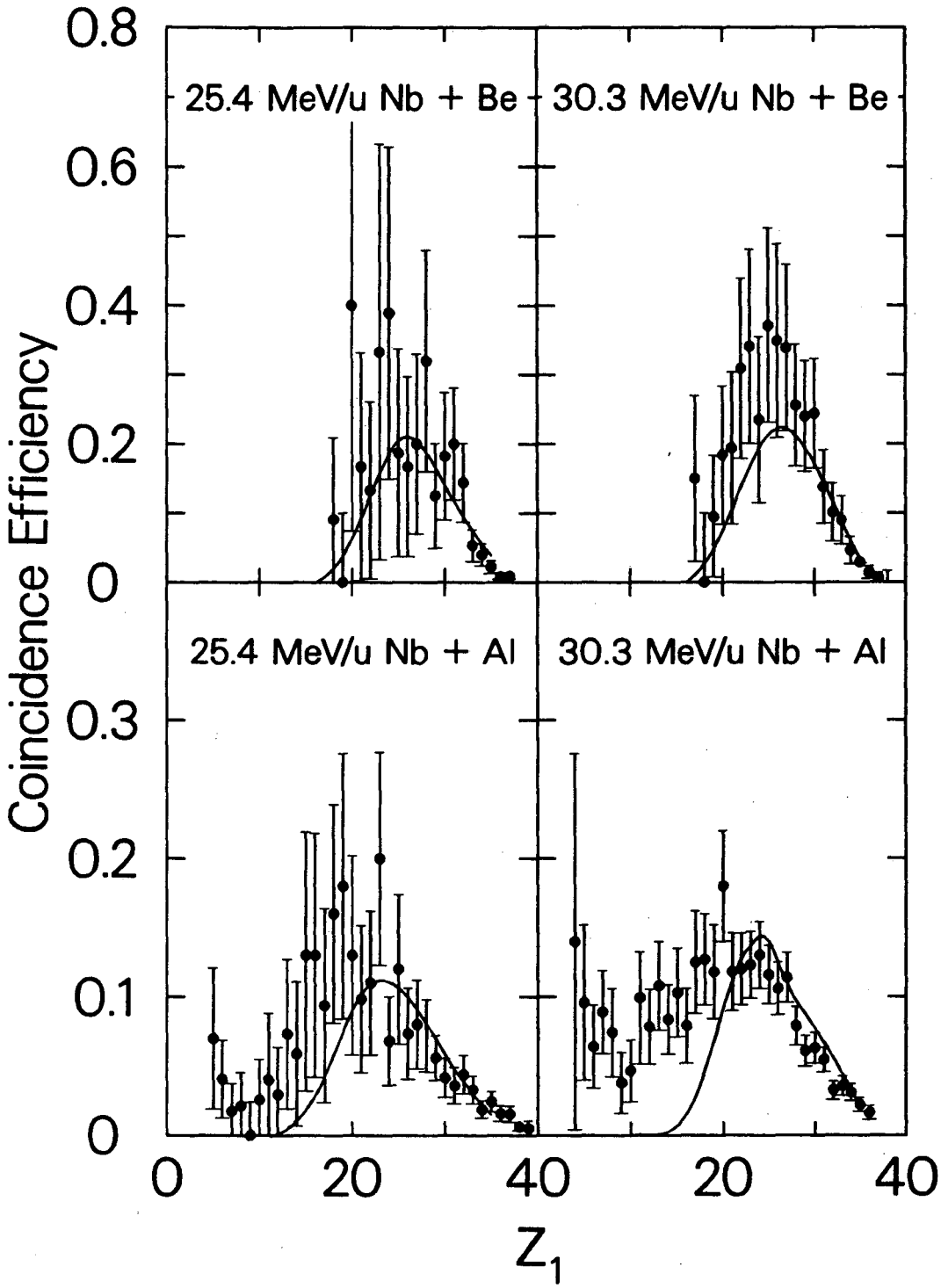

XBL 875-2332

Fig. 18

LAWRENCE BERKELEY LABORATORY
TECHNICAL INFORMATION DEPARTMENT
UNIVERSITY OF CALIFORNIA
BERKELEY, CALIFORNIA 94720